

Impact of future climate and emission changes on stratospheric aerosols and ozone

G. Pitari¹, E. Mancini¹, V. Rizi¹, and D.T. Shindell²

¹Dipartimento di Fisica, Università de L'Aquila, 67010 Coppito, L'Aquila, Italy

²NASA Goddard Institute for Space Studies, 2880 Broadway, New York, NY 10025, USA

Manuscript submitted to
Journal of Atmospheric Sciences
June 21, 2001

Correspondence to: Giovanni Pitari
Dipartimento di Fisica, Università de L'Aquila, via Vetoio, 67010 Coppito, L'Aquila - Italy.
E-mail: gianni.pitari@aquila.infn.it

Abstract

Global climatological distributions of key aerosol quantities (extinction, optical depth, mass and surface area density) are shown in comparison with results from a three-dimensional global model including stratospheric and tropospheric aerosol components. It is shown that future trends in global and regional anthropogenic emissions of sulfur dioxide may induce substantial changes in the lower stratospheric budget of sulfate aerosols: with the IPCC-SRES (2000) upper limit ‘A2’ scenario, the integrated stratospheric sulfate mass is predicted to increase from 0.15 Tg-S to 0.20 Tg-S in year 2030, and the $1.02\ \mu\text{m}$ average optical depth from 1.5×10^{-3} to 2.2×10^{-3} with a 50% increase in short wave radiative forcing. The latter, in turn, is found to be about 23% the total forcing by sulfate aerosols (tropospheric + stratospheric). Convective upward transport of sulfur dioxide to the tropical tropopause is found to be a key point for understanding the global distribution of sulfate in the lower stratosphere. Large increases of anthropogenic sulfur production at tropical latitudes by developing countries may explain these rather large predicted changes of stratospheric sulfate. Effects of future climate changes on stratospheric aerosols are also discussed: it is shown that the largest perturbation is on the probability of polar stratospheric cloud (PSC) formation, and that is driven primarily by greenhouse gas-induced temperature changes. In particular, the model calculated wintertime Arctic increase of total aerosol optical depth is close to a factor of 2, with PSC optical depth and surface area density increasing by a factor of 5. This is mainly due to the predicted decrease of sudden stratospheric warming frequency in the Northern Hemisphere and the associated higher stability of the polar vortex. Enhanced

ozone losses result from faster heterogeneous chemical reactions on both sulfate and PSC aerosol surfaces. The chemically-driven total ozone recovery in 2030 relative to 2000 is predicted to decrease from +4.5% to +3.7% when taking into account both climate and surface emission changes: effects related to climate changes (perturbed stratospheric circulation, water vapor distribution, PSC frequency, etc.) account for about 2/3 of the calculated slow down of the O₃ recovery rate.

1 Introduction and experiment setup

The main process responsible for stratospheric sulfate aerosol (SSA) production is sulfuric acid (H_2SO_4) and water condensation on pre-existing nuclei transported from the tropopause or formed in-situ through homogeneous nucleation mechanisms. Stratospheric sulfuric acid, in turn, is formed by in-situ oxidation of sulfur dioxide (SO_2) via a three-body reaction with the hydroxyl radical (OH) (Turco, 1992; Weisenstein et al., 1997).

Sulfur dioxide can be both transported from the tropical tropopause, where it is efficiently uplifted from the boundary layer by deep convection (Rodhe, 1985), or photochemically produced in the mid-stratosphere after UV photolysis of carbonyl sulfide (OCS). The latter species has a very long lifetime (about 25 years in the troposphere and 85 years in the stratosphere) because oxidation by atomic oxygen and OH are slow (JPL, 1997). OCS is photodissociated once it reaches the stratosphere, becoming an important precursor for stratospheric sulfate aerosols. Carbonyl sulfide originates at the ground by natural biogeochemical cycling of sulfur and its flux is rather small, as are removal rates close to the boundary layer (Andreae, 1985). Measurements indicate that this precursor is well mixed in the troposphere with a typical mixing ratio of 500 pptv (Carrol, 1985; Inn et al., 1979).

Sulfur dioxide, on the other hand, is the main precursor of tropospheric sulfate (SO_4^-). It comes from both natural sources (volcanoes, oceans, biomass burning) and anthropogenic activity (fossil fuel burning, in-situ emissions from aircraft). Oceanic SO_2 is formed through oxidation of dimethyl sulfide (DMS) via reaction with OH and NO_3 (Feichter et al., 1996). About 65-75% of tropospheric sulfur is of anthropogenic origin: independent estimates are those of Spiro et al. (1992) (76%), Bates et al. (1992) (74%), Graf et al. (1997) (66%), IPCC-TAR (2001) (66%): this average fraction, however, may have large regional variations, with peaks located over Northern

Hemisphere mid-latitude continental sites. This may potentially imply a strong impact of future emission changes of anthropogenic sulfur, both globally and on regional scales, on stratospheric sulfate aerosols, with effects on radiation and ozone photochemistry.

In this paper results of a three-dimensional global chemical-transport model (CTM) are shown to explore the sensitivity of stratospheric sulfate on anthropogenic sulfur emissions, including subsonic aircraft. A climate model is coupled off-line to the CTM in order to study future trends of stratospheric aerosols produced by climate changes due to greenhouse gas (GHG) increase in the future atmosphere. These aerosol perturbations are due to stratospheric circulation changes and to perturbed distributions and abundance of gas species, such as water vapor and nitric acid, that may affect the formation of polar stratospheric cloud (PSC) and H_2O - H_2SO_4 aerosol particles. The final modeling step is to analyze future trends of ozone with and without aerosol changes produced by climate and emission changes.

The strategy of this work has been first to validate present time model results for key quantities and species (aerosol extinction, optical depth, mass, surface area density; H_2O and HNO_3 stratospheric distributions) using available satellite data (SAGE-II for aerosol, HALOE for H_2O and CLAES for HNO_3) and then to predict future changes of stratospheric sulfate and PSCs. Table 1 summarizes all steady-state numerical experiments conducted for this study. Comparison of ‘NA’, ‘OCS’ and ‘TRP’ experiment results with 2000-baseline allows us to better understand the relative role of different contributions to SSA. Comparison of 2030-CH with 2000-baseline shows the effects of chemistry changes, while ‘B1’ and ‘A2’ cases explore the SSA sensitivity to sulfur emission changes. Finally, experiments ‘TC’ and ‘TS’ provide results of future climate changes on stratospheric aerosols (PSC in particular).

The paper is organized in six blocks: after this introduction (1), a description of the modeling

tools follows (2), including a microphysical module for aerosol formation and growth; then a model validation and discussion of future changes of SSA (3) and PSC (4) is presented, with a summary of ozone results (5); the main conclusions are summarized in the last section (6).

2 Model description

The model used here is a low-resolution three-dimensional (3D) climate-chemistry coupled model, that will be identified hereafter as ULAQ model ("University of L'Aquila"). The chemical-transport module uses a $10^\circ \times 20^\circ$ resolution in latitude-longitude and 26 log-pressure levels, from the ground to about 0.04 hPa, with an approximate resolution of 2.84 km. Dynamical fields (streamfunction, velocity potential and temperature) are taken from the output of a spectral general circulation climate model (GCM) (Pitari, 1993). The vertical velocity is calculated from the horizontal divergence. A flux-form Eulerian fully explicit advection scheme is used, with one hour time-step, used for both dynamics and chemistry. Relative humidity, cloud distribution and net precipitation rates are taken from climatological data, i.e. Oort (1983), Rossow et al. (1987), Shea (1986). The coupling between CTM and GCM is made via the dynamical fields (GCM \Rightarrow CTM) and via the radiatively active species (H_2O , CH_4 , N_2O , CFCs, O_3 , NO_2 , aerosols: CTM \Rightarrow GCM).

A small horizontal diffusion is used for numerical stability purposes, being about $10^6 \text{ m}^2/\text{s}$ in the troposphere and $2 \times 10^5 \text{ m}^2/\text{s}$ in the stratosphere at mid-high latitudes. Corresponding values in the tropics (20S-20N) are one order of magnitude smaller. A vertical diffusion coefficient K_{zz} is used to simulate those transport processes not explicitly included in the model. K_{zz} is assigned with large values in the boundary layer ($10 \text{ m}^2/\text{s}$) decreasing to $0.1 \text{ m}^2/\text{s}$ in the lower stratosphere at mid-high latitudes and to $0.02 \text{ m}^2/\text{s}$ in the tropics. The effect of gravity wave

breaking is simulated by increasing K_{zz} in the upper stratosphere and mesosphere and using a Rayleigh friction coefficient in the circulation model. The scheme adopted for tropospheric deep convection takes inspiration from that described in Muller and Brasseur (1995): the rate at which a chemical compound is transported at a given altitude in the free troposphere is calculated as a function of a convective uplift rate and the species mixing ratio in the boundary layer. Here the convective rate is not explicitly calculated in terms of cumulonimbus cover fraction and cloud top altitude, but is assumed to be linearly related to the NO_x lightning production calculated in the ECHAM4 general circulation model (Grewe et al., 2001).

The GCM is widely described in the literature. For details on the major dynamical features (temperature, wind fields, planetary waves, sudden warmings, radiation, surface temperature balance) and on the ozone prediction capabilities (transport, mid-latitude heterogeneous chemistry, polar chemistry, ozone hole, trends) we refer to published papers: Pitari et al. (1992); Pitari (1993). The three-dimensional CTM has been used and validated in NASA (1999); Pitari et al. (2001); Bregman et al. (2001).

All chemical species are diurnally-averaged; diurnal variations of N_2O_5 are parameterized following Brasseur and Solomon (1984), including also removal from heterogeneous reactions on both sulfate aerosols and PSCs. Some species are assumed to be present only during daytime (O , $\text{O}(^1\text{D})$, H , OH , HO_2 , NO , Cl , ClO , Br , BrO). The 24-hr averaged photodissociation rates are calculated daily (i.e. every 24 model hours) and include the effects of Rayleigh and Mie scattering. All medium and short-lived chemical species are grouped in families: O_x ($\text{O}_3 + \text{O} + \text{O}(^1\text{D})$), NO_y ($\text{NO}_x + \text{HNO}_3$), NO_x ($\text{NO} + \text{NO}_2 + \text{NO}_3 + 2\text{N}_2\text{O}_5 + \text{HNO}_4 + \text{PAN} + \text{ClONO}_2 + \text{BrONO}_2$), HO_x ($\text{H}_2\text{O}_2 + \text{HO}_2 + \text{OH} + \text{H}$), CHO_x ($\text{CH}_3\text{O}_2 + \text{CH}_3\text{OOH} + \text{CH}_2\text{O}$), Cl_y ($\text{Cl} + \text{ClO} + 2\text{ClOOCl} + \text{HOCl} + \text{ClONO}_2 + \text{HCl}$), Br_y ($\text{Br} + \text{BrO} + \text{HOBr} + \text{BrONO}_2 + \text{HBr}$),

SO_x ($\text{SO}_2 + \text{H}_2\text{SO}_4$), aerosols. Long-lived and surface-flux species included in the model are N_2O , CH_4 , H_2O , CO , C_2H_6 , C_2H_4 , C_3H_6 , C_5H_8 , $\text{C}_{10}\text{H}_{16}$, other hydrocarbons, CFCs, HCFCs, halons, OCS, CS_2 , DMS, H_2S , SO_2 for a total of 40 transported species (plus 57 aerosol size categories) and 26 species at photochemical equilibrium. Photochemical terms are calculated with the same time frequency of advective tendencies. All photochemical data are taken from JPL (1997), including the most important heterogeneous reactions on sulfate and PSC aerosols.

The ULAQ model includes the major components of tropospheric aerosols (sulfate, carbonaceous, dust, sea salt). The size distribution of sulfate (both tropospheric and stratospheric) and PSC aerosols, made in our model of nitric acid trihydrate (NAT) and water ice, are calculated using a fully interactive and mass conserving microphysical code for aerosol formation and growth. Denitrification and dehydration due to PSC sedimentation are calculated explicitly from the NAT and ice aerosol predicted size distribution. The aerosol microphysical code has been described in Pitari et al. (1993) in a two-dimensional (2D) framework; the same code (including also bimolecular homogeneous nucleation for H_2O – H_2SO_4) has then been adapted for the three-dimensional CTM. The main difference with respect to the 2D framework is that here all microphysical calculations are made explicitly on the whole 3D grid, so that no more use is done of condensation and nucleation probabilities related to the temperature distribution along a latitude circle. A full coupling with chemistry insures total sulfur, water and NO_y mass conservation, except of course for the net loss determined by sedimentation and wet/dry depositions.

Bimolecular homogeneous nucleation (not included in Pitari et al. (1993)) represents one of the most important sources of new sulfate aerosols in the upper tropical troposphere and possibly also in the polar vortices, where low temperatures may dramatically increase the sulfuric

acid saturation ratio. Homogeneous nucleation is also very important when the stratospheric abundance of sulfur is greatly perturbed by SO_2 injection from large explosive eruptions (Pinto et al., 1989). In occasion of great volcanic events, the H_2SO_4 vapor pressure is so high that a large fraction of new stratospheric aerosol particles are formed by means of homogeneous nucleation. It should be mentioned that other sources of new aerosol particles are now proposed to be even more important than homogeneous nucleation, in particular the ion-ion recombination mechanism (Turco et al., 1998). At the present stage, however, our model does not include this kind of process.

The parameterization of homogeneous nucleation from a binary system (H_2SO_4 and H_2O) is based on the works of Hamill et al. (1977) and Steele and Hamill (1981). The homogeneous nucleation rate can be calculated according to:

$$J(T) = 4\pi r^{*2} \beta_A N_B \exp\left(-\frac{\Delta G^*}{kT}\right) \quad (1)$$

where β_A represents the molecular flux of gas A (H_2SO_4) to the droplet, N_B the molecular density of gas B (H_2O), k is the Boltzmann constant, T the temperature, r^* the critical radius of nucleating molecular clusters and ΔG^* is the corresponding free energy barrier. ΔG^* is in turn a function of A and B saturation ratios; for more details we refer to Ricciardulli et al. (1996) and Weisenstein et al. (1997).

Aerosol particles are divided in size bins, and each one of this size categories are separately transported: in the model there are 15 bins for sulfate (from about 0.4 nm up to 10 μm by doubling the radius), 9 bins for NAT (0.08 μm to 20 μm), 9 bins for ice (0.16 μm to 40 μm), 6 bins for black carbon (5 nm to 0.16 μm), 6 bins for organic carbon (0.01 μm to 0.32 μm) and finally 6 bins for both dust and sea salt particles (0.32 μm to about 10 μm). Sulfate aerosols are allowed in the model to interact with carbonaceous particles, through coagulation and heterogeneous

nucleation and may become condensation nuclei for NAT particles. Surface fluxes of SO₂, DMS, black carbon, organic carbon and mechanically generated particles are those provided for the IPCC-TAR (2001) assessment. Future anthropogenic SO₂ fluxes are those recommended by IPCC-SRES (2000) for upper and lower limit scenarios ('A2', 'B1', respectively).

Washout of soluble gases and aerosol particles is parameterized as a first-order loss rate, calculated as a function of the precipitation rate:

$$R(\phi, \lambda, z, t) = 6 \times 10^{-8} w P(\phi, \lambda, t) v(\phi, \lambda, z, t) \quad (2)$$

where R is the in-cloud washout rate, P is the precipitation rate (mm/month) taken from monthly-averaged climatological data of Shea (1986), v is the vertical distribution of washout, ϕ, λ, z, t are latitude, longitude, log-pressure vertical coordinate and time of the year, respectively, and w is a dimensionless factor related to species solubility (Muller and Brasseur, 1995) (for SO₄⁼ and SO₂ we use 1.5 and 0.5, respectively). The washout vertical distribution is calculated using the climatological distribution of cumulonimbus and nimbostratus clouds:

$$v(z) = \frac{f_1(z)c_1 + f_2(z)c_2}{c_1 + c_2} \quad (3)$$

where c_1, c_2 are the fractional cover of cumulonimbus and nimbostratus at a given location and f_1, f_2 are factors decreasing from one (in the cloud center) to zero (at cloud top and base) (Muller and Brasseur, 1995). A comparison of calculated annual mean sulfate wet deposition fluxes with available observations (see Feichter et al., 1996) is presented in Table 2; this model validation is particularly significant, being wet deposition the primary loss mechanism for tropospheric sulfate. At least on the annual basis, the calculated regional distribution of sulfate wet removal is consistent with climatological observations, except for some underestimation over Europe.

An additional sink is included for aerosol particles in the upper troposphere, at altitudes

where ice clouds may form. It is beyond the purposes of the present study to include in the model a realistic description of the ice nucleation mechanism, so that we chose to parameterize it in a simplistic way, using a prescribed aerosol removal rate of 10^{-6} s^{-1} decreasing to zero towards the tropopause. This may be regarded as the major uncertainty in our simulation of troposphere - stratosphere exchange of sulfate particles, along with the validity of the scavenging parameterization in the upper troposphere.

3 Stratospheric sulfate aerosol

Stratospheric sulfate aerosols are usually supercooled liquid solutions of H_2O and H_2SO_4 , with sulfuric acid mass in the particles ranging between about 40% and 90% depending on temperature and specific humidity. The observed size distributions of these particles results from the action of several microphysical processes (Turco et al., 1979), such as gas condensation, homogeneous and heterogeneous nucleation, evaporation, coagulation, gravitational sedimentation along with large-scale transport. Particles can be removed by wet deposition once they penetrate downward the mid-high latitude tropopause. This downward tropopause flux is mainly produced by vertical advection, which is faster than gravitational sedimentation, at least for submicron particles. Sedimentation, however, is important for determining the aerosol vertical profile and size-distribution in the mid-stratosphere.

Background sulfate aerosols are those photochemically produced in steady-state conditions of stratospheric sulfur abundance. Model calculations (see ahead) show that in this normal “background” conditions about 43% of stratospheric sulfate is originated by OCS photolysis. Another 27% comes from SO_2 feeding the stratosphere from the tropical tropopause, where it is convectively uplifted from the boundary layer. The remaining 30% is upward transported

tropospheric sulfate. These numbers are obtained after integrating over the whole stratosphere, with lower boundary at the thermal tropopause. Moving the boundary by 3 km above it, the OCS production fraction raises to about 50%, pointing out to a sharp SO₂ gradient immediately above the tropopause.

These background sulfate particles are often perturbed by new aerosol formation starting from SO₂ or H₂S injected in-situ by explosive volcanic eruptions. In case of large eruptions the aerosol optical thickness may increase by orders of magnitude. Sporadic sulfur injection in the stratosphere produced by large explosive volcanic eruptions has the potential to produce climatic changes in a time frame of a few years (Hansen et al., 1992) and also catastrophic ozone losses (Prather, 1992; Randel et al., 1995). The stratospheric e-folding lifetime of these volcanic particles is of the order of one year (Weisenstein et al., 1997; Grant et al., 1996), so that for events of magnitude comparable to El Chichón or Pinatubo at least 3-4 years are necessary to recover the unperturbed background loading of SSA.

Stratospheric aerosols have been sampled using balloons and high-altitude aircraft and from ground based lidar measurements. The most extensive coverage of stratospheric aerosols has been made by the SAGE-II satellite instrument: the use of these data has provided information on the global scale distribution of several aerosol properties, as extinction, optical thickness, mass and surface area density, acidity, and size distribution (McCormick et al., 1979; Yue et al., 1994). SAGE-II data are now available on the web (<http://www-sage2.larc.nasa.gov>) in two versions: stratospheric data (Kent et al., 1993; Thomason et al., 1997) from 5.5 to 40.5 km, and revised tropospheric data (Kent et al., 1998), from 6.5 up to 25.5 km altitude. These observations have been averaged over volcanically quiet years (December 1988-November 1989; June 1996-May 1998) and are used here to validate the previously described CTM including

SO_x chemistry, stratospheric and tropospheric aerosol components and the microphysics code for sulfate and PSC particles.

The calculated annually averaged zonal distribution of SO₂ (Fig. 1a) shows large mixing ratios at the tropical tropopause (about 35 pptv) that are produced by convective uplift from the surface; the sharp gradient in the lower stratosphere is due to SO₂ oxidation by OH. Upper tropospheric values are in the range of (sparse) measurements (10-300 pptv) and are close to independent 3D calculations (Langner and Rodhe, 1991) (Fig. 2b). Vertical profiles shown in Fig. 2(a,b) clearly show that deep convection uplift is the primary mixing mechanism for tropospheric SO₂ (Langner and Rodhe, 1991; Rodhe, 1985) and is particularly efficient in the tropics and over mid-latitude continental sites during summertime. Future trends of anthropogenic sulfur released in the tropics will then affect the amount of upper tropospheric SO₂ available for upward transport in the stratospheric tropical pipe. The equatorial maximum at 30 km (about 40 pptv) is produced by OCS photolysis, while the sharp increase above 35 km is due to particle evaporation and H₂SO₄ photolysis. Similarly, the calculated SO₄⁻ mixing ratio peak below 30 km (Fig. 1b) is related to OCS photolysis producing mid-stratospheric SO₂. The negative gradient immediately upwards is due to particle sedimentation, while the secondary maximum at 40 km is caused by reformation of gas-phase H₂SO₄ from particle evaporation. The negative gradient above this height is due to sulfuric acid photolysis. The sulfate minimum in the upper troposphere results from efficient washout removal below about 400 hPa and from the parameterized sulfate particle sink due to upper tropospheric ice nucleation.

A validation of the deep convection parameterization adopted in the model has been made with available observations and independent calculations of the vertical distribution of Rn-222, which is an ideal tracer to test this type of vertical transport, due to its rather short and well

established radioactive lifetime. Results are shown in Fig. 2(c, d) and are close to those obtained in the tropics in the 3D simulation by Feichter and Crutzen (1990) who used a more detailed and ‘physically based’ convection scheme. As expected, inclusion of deep convection has the effect to decrease the tracer concentration in the boundary layer and to increase it by an order of magnitude (and even more) above 500 hPa in the Northern Hemisphere summer mid-latitudes and above 300 hPa in the tropics. These results suggest that in these regions deep convection is the dominant redistribution process. A comparison with mid-latitude observations is made in Fig. 2d: data are taken from the Liu et al. (1984) climatology at 23 continental mid-latitude sites. Only the average profile for summer is statistically significant, due to its high variability in the mid-troposphere (depending essentially on convective events) and the small number of profiles for the other seasons (Jacob and Prather, 1990).

Extinction profiles calculated in the model are compared to SAGE-II data (at $\lambda = 1.02 \mu\text{m}$) in Fig. 3 and Fig. 4. Mass to extinction conversion is calculated assuming stratospheric sulfate aerosols as $\text{H}_2\text{O-H}_2\text{SO}_4$ solutions with 70% sulfuric acid weight fraction and running a Mie scattering program to get the Q_{ext} parameter as a function of particle radius. The model predicted size-distribution is then used at each grid point to get the extinction at the given wavelength ($1.02 \mu\text{m}$ in this case). The comparison shows that the model does an excellent job in the stratosphere and is also capable to reproduce the fast extinction increase at mid-latitudes from January to April in the mid-troposphere. Some model overestimation, however, is present in the Northern Hemisphere subtropics below the tropopause, pointing out to a probably unrealistic abundance of soil dust submicron particles coming from the Sahara region. In addition, the model does not show enough high-latitude subsidence above 25 km (see also Table 3) and underestimates the January maxima at 20 km by nearly a factor of two.

The good model performance shown in Fig. 3 and Fig. 4 is corroborated also by surface area density (SAD) climatological values for sulfate particles (Thomason et al., 1997). CTM values are obtained from the calculated sulfate aerosol size distribution for particles larger than $0.05\ \mu\text{m}$, in order to include only the contribution of optically active particles to the geometric surface area density and make a more meaningful comparison to SAGE-II derived values. Results are shown in Fig. 5 and Fig. 6. The model is able to reproduce the calculated SAD maximum poleward of 40° latitude in the 10-13 km layer. This maximum is close to $2 \times 10^{-8}\ \text{cm}^{-1}$ and may be largely explained as a result of the large-scale transport accumulation in the mid-high latitude lower stratosphere. Differences in the polar stratosphere may be explained in terms of polar subsidence and may also reflect the fact that SAD is not a pure dynamical tracer, but its distribution is affected by the presence of local net aerosol production (coagulation of ultrafine particles produced by homogeneous nucleation in the polar vortices, nitric acid nucleation, etc.). When the model includes the aircraft contribution to the sulfur budget, a difference of about $1.0\ \mu\text{m}^2/\text{cm}^3$ is present poleward of 50N at 11 km of altitude. About 30% of this additional contribution to SAD comes from particles larger than 50 nm, which result from large scale gas phase condensation of aircraft generated sulfuric acid and from coagulation of ultrafine particles directly formed in aircraft plumes.

The model calculated mass, integrated above the tropopause, is found to be 0.151 Tg-S, remarkably close to the 0.156 Tg-S obtained from the 1979 observed stratospheric optical depth ($\tau = 12.5 \times 10^{-4}$) from Kent and McCormick (1984). Conversion to sulfate mass of the SAGE-II τ value is made assuming $1.1 \times 10^3\ \text{m}^2\ \text{kg}^{-1}$ as mass-extinction factor (K_e), an average 65% sulfuric acid weight fraction for stratospheric aerosols and a 20% correction factor for including also the 2 km layer immediately above the tropopause. SAGE-II data, in addition, do not show

any significant trend in the lower stratosphere region in the last 15 years (excluding volcanic contributions). This result is not surprising if we take into account that global anthropogenic sulfur production has declined over Europe and North-America and has increased over Northern China, with relatively small changes in the critical tropical region. Air traffic, on the other hand, can only be significant for surface area density, while in terms of stratospheric sulfate mass (and optical depth) the contribution of the whole subsonic aircraft fleet is only of the order of few percents (see ahead).

A comparison in terms of optical depth is shown in Table 3 for the altitude layers 10-15 km (tropopause), 15-20, 20-25, 25-30 km. At the tropopause layer, the optical depth has a minimum in the tropics and then increases towards the polar regions. The models overestimates τ in the Northern Hemisphere subtropics, due to some large contribution from tropospheric submicron soil particles. Above the tropopause the latitudinal gradient of τ is much flatter, and the $1.02\ \mu\text{m}$ optical depth stays always close to 10^{-3} , as observed. These results suggest that the stratospheric and upper tropospheric size distribution of particles is captured correctly, and this is a consequence of realistic fluxes and removal mechanisms for both SO_2 and $\text{SO}_4^{=}$, along with a correct simulation of convective uplift in the tropical troposphere and large scale transport in the lower stratosphere.

The model has also been validated in terms of tropospheric sulfur chemistry, that we will see is important for understanding future changes of SSA. In Table 4 model budgets are compared with average results from the COSAM exercise (IPCC-TAR, 2001), where 11 tropospheric sulfate models were compared. There is a good agreement in terms of mass, removal, sources, lifetime and efficiency (or potential). The latter is the rate at which released sulfur ends up in sulfate (the exact definition is sulfate burden divided by sulfur source). The best estimate

for this potential is 2.6 days. Our model, however, predicts a longer lifetime for SO_2 (2.1 days versus 1.6) because a slower dry deposition rate on land has been used (0.1 cm/s), following recent suggestions in the literature (Ganzeveld et al., 1998; Lohmann et al., 1999).

A number of sensitivity studies are made to investigate possible changes of SSA in future years with changing chemistry and sulfur emission scenario (see Table 1). The sensitivity to present time sulfur precursor abundance is also studied. Table 5 summarizes the stratospheric SO_4^- response in these cases: the anthropogenic flux is 69 Tg-S/yr for 2000, 53.5 Tg-S/yr for 2030-B1 and 112 Tg-S/yr for 2030-A2, and is zero in the case where only OCS is considered as sulfur precursor. The natural flux is 41 Tg-S/yr (26 from DMS, 9.6 from non explosive volcanoes, 5.4 from soils and biomass burning) plus a constant mixing ratio of 500 pptv for surface OCS. The SAGE-II derived mass, integrated above the tropopause, is 0.156 Tg-S with an optical depth of 15×10^{-4} at $1.02 \mu\text{m}$ and a total H_2O - H_2SO_4 mass of 0.72 Tg (we have used the 1979 volcanically-quiet estimates reported in Kent and McCormick (1984), including a 20% correction factor necessary to take into account the 2 km layer immediately above the tropopause, as suggested by the authors themselves). Our model predicts 0.151 Tg-S for 2000 including subsonic aircraft emission of sulfur dioxide, 0.147 Tg-S without aircraft (-3%), 0.065 Tg-S with only OCS as sulfur precursor (-57%), 0.046 Tg-S not considering any photochemical source of sulfate above the tropopause (-70%) and 0.204 Tg-S for 2030-A2 (+35%). These relative changes may be somehow different when calculated from H_2O - H_2SO_4 mass or optical depth, in particular for 2000-OCS and 2000-TRP cases, reflecting the fact that the average stratospheric weight fraction of sulfuric acid may be larger (as in ‘OCS’) or smaller (as in ‘TRP’) than in the baseline case.

These model calculations, taking into account both stratospheric and tropospheric sulfate chemistry, show that stratospheric sulfate originating from OCS photolysis accounts for about

43% of the total. About 27% comes from SO_2 feeding the stratosphere via the tropical tropopause, where it is convectively transported from the surface. The remaining 30% is upward transported tropospheric sulfate. If we remind that anthropogenic sulfur accounts for about 70% of the total and that a 62% increase of anthropogenic SO_2 emissions are projected in the 2030-A2 scenario, we may largely explain the 35% SSA increase predicted for this future scenario.

The slight SSA mass increase in case 2030-B1 with respect to 2030-CH (+1%) means that the regional distribution of sulfur emissions is also important, along with the integrated value (the latter here decreases by 15.5 Tg-S/yr). The slight increase in case 2030-CH with respect to the 2000 baseline case (+6%) is due to more stratospheric OH, because of increasing CH_4 and O_3 recovery, and to the increasing subsonic air-traffic. The largest SSA perturbation with respect to 2000-baseline (+35%) is found in case 2030-A2: here regional emission changes are coupled to the projected upper limit increase of the total anthropogenic sulfur flux. In this case the calculated tropopause short wave radiative forcing reaches -0.186 W/m^2 , with a 48% increase with respect to 2000-baseline. Table 6 summarizes the SSA budgets and compares them to the total (stratosphere+troposphere) budgets. Stratospheric sulfate accounts for about 16% of the total; SSA mass is about 10% the total sulfate aerosol mass, because large hygroscopic growth is possible in the troposphere when relative humidity is larger than 40%. Optical depth in the stratosphere is about 7.5% of the total τ due to sulfate aerosols, but the resulting short wave radiative forcing is about 23% of the total.

Fig. 7 shows zonally averaged total sulfur emission for scenarios 2000, 2030-B1, 2030-A2. Pollution regulation in mid-latitude western industrialized countries are decreasing the amount of released SO_2 , while the opposite is taking place in developing countries, mostly located at tropical latitudes (India, China, Middle-East, Africa, Center and South-America). Even in case

B1 (decreasing total emission) the amount of sulfur emitted in tropical latitudes is higher than in 2000. Fig. 8 is a 2D view of these emissions for 2000 and for the 2030 upper limit case ('A2'), showing more clearly the above described regional trends. Our study indicates that these increasing tropical emissions of anthropogenic sulfur may be responsible of significant changes of SSA mass and surface area density, through efficient convective uplift of surface SO_2 up to the tropical tropopause, where the middle atmosphere is fed from through the stratospheric tropical pipe. Predicted SAD changes are shown in Fig. 9 along with mass density changes: increases up to $0.5 \mu\text{m}^2/\text{cm}^3$ for SAD and $50 \text{ ng}/\text{m}^3$ are found in the Northern Hemisphere between 100 and 200 hPa. This increase of SAD may be important for the lower stratospheric ozone photochemistry, via heterogeneous chemical reactions involving NO_x and chlorine and bromine oxides.

4 Polar stratospheric clouds

Common to most modelling studies (Pitari et al., 1993 as an example) is the assumption of the existence of two types of solid phase PSC particles, forming at certain threshold temperatures (e.g. NAT condensation temperature and the ice frost point). Subsequent research has revealed the existence of at least three PSC particle types, showing complicated transition processes between liquid and solid type particles which depend on the temperature histories of individual particles (Larsen, 2000). The most important physico-chemical processes involved in the current understanding of PSC formation and growth are the evolution of liquid PSC and the mechanisms of liquid to solid and solid to liquid transitions. The purpose of the present study is not to study PSC particles evolution in a rigorous microphysical approach, but to estimate the magnitude of future changes in the frequency of occurrence of these aerosols. This is done using a rather

simple scheme for the particle formation (i.e. threshold temperatures for solid phase NAT and water ice particles), but keeping a correct representation of the environmental key processes controlling the budgets of solid phase HNO_3 and H_2O in the polar stratosphere, i.e. temperature and local gas-phase abundance. For details on the microphysical scheme adopted for NAT and water ice aerosols we refer to Pitari et al. (1993). The main difference is that the scheme was adjusted there to a zonally averaged framework, with the introduction of a statistically derived probability of condensation for NAT and ice, while here heterogeneous nucleation on sulfate aerosols and gas condensation/evaporation are treated ‘naturally’ at each 3D grid-point.

Mass, surface area and optical depth of PSCs are calculated in the microphysical module of the CTM from a discretized size distribution (from $0.08\text{ }\mu\text{m}$ up to about $40\text{ }\mu\text{m}$ by doubling the radius) and taking into account gas-particle interactions, so that future changes of water vapor driven by temperature trends at the tropical tropopause are taken into account in model predictions, as well as the stratospheric nitric acid increase produced by positive trends of N_2O production. Stratospheric cooling due to future GHG increase is, however, the most important factor affecting the amount of PSCs in the polar lower stratosphere.

Increasing GHG concentration warms the Earth’s surface, but cool the stratosphere radiatively, thus affecting chemistry through both homogeneous and heterogeneous reactions. Heterogeneous chemistry is very sensitive to temperature, not only because the probability of reactions involving chlorine compounds is highly dependent on sulfate aerosol acidity (which in turn is a function of humidity and temperature), but also because the frequency of PSC occurrence in the polar regions may greatly increase in a colder stratosphere. In addition, the amount of PSC aerosols in the polar vortices may change as a consequence of water vapor and nitric acid changes in the stratosphere (IPCC, 1999), due to trends of CH_4 and N_2O and warming/cooling

of the tropical tropopause.

Experiment ‘TC’ of Table 1 and Table 5 is the one including temperature and dynamical fields appropriate for the year 2030, as calculated in the ULAQ climate model. Fig. 10 compares the ULAQ mean zonal temperature change for March with the corresponding field calculated in the Global Climate/Middle Atmosphere Model (GCMAM) of the Goddard Institute for Space Study (GISS). The basic features of these temperature anomalies are: (a) tropospheric warming with maxima in the tropics (~ 4.5 K) at about 350 hPa in ULAQ and 250 hPa in the GISS model; (b) a warmer tropical tropopause; (c) stratospheric cooling with peak values in the Arctic vortex (see also WMO (1999) for a discussion of this point). Both features (b)-(c) are more pronounced in the GISS model, where the tropospheric warming penetrates into the tropical lower stratosphere up to about 50 hPa.

The tropical upper tropospheric warming maximum is mainly produced by convective heating, and we should remind here that this feature is not present (or is smaller) in some other GCM simulations: it is then important to keep in mind that some findings of the present work could be partly model-dependent. We also note that differences of the ULAQ ΔT with respect to Pitari et al. (1992) are not surprising, due to the fact the previous ULAQ simulation did not include an explicit parameterization of tropospheric heating processes (including convection), but used a Newtonian cooling approximation.

WMO (1999) has compared model temperature responses in future climate conditions, showing that all the models available for this analysis (4 in total) give a temperature response which is qualitatively similar to the GISS GCMAM. We may conclude that although not all climate models give similar results, the tropical upper tropospheric warming maximum in the GISS (or ULAQ) model is not the unique behavior of a single GCM, but seem relatively robust across

several models. A recent paper by Shindell et al. (2001) presents some observational evidences in support of the changes seen in the GCMAM. It is shown that the thermal and dynamical changes in the model capture the behavior of the real atmosphere in the Northern Hemisphere winter reasonably well.

Mean zonal temperature alone cannot fully explain, however, local changes in the probability of PSC formation. Fig. 11 is a lat/lon view of the calculated temperature at 20 km in the Northern Hemisphere winter: while in the present time simulation the minimum Arctic temperature is between Iceland and Greenland (~ 194 K), in future climate conditions (2030) the minimum moves westward and is located between Greenland and Northern Canada (~ 189 K). The tropospheric warming shown in Fig. 10 has the effect to increase the atmospheric stability, so that the propagation of planetary waves in the wintertime stratosphere is altered and the frequency of sudden stratospheric warmings in the Northern Hemisphere is reduced. On this aspect the ULAQ climate-chemistry model behaves similarly to the GISS model, with the net result to have a more stable Arctic vortex in future climate conditions. Fig. 12 shows the wintertime Northern Hemisphere anomalies of the amplitude of geopotential wavenumbers 1 and 2 as predicted in the ULAQ model for 2030-2000: the generalized wave amplitude decrease in the stratosphere is a consequence of the enhanced atmospheric stability.

The number concentration and size distribution of PSC aerosols are a function of water vapor and nitric acid saturation ratios, so that not only the temperature threshold for NAT and water ice formation is important, but also the local amount of H_2O and HNO_3 . The ULAQ model calculates the stratospheric distributions of these gases taking into account the most important physical and chemical mechanisms: saturation water vapor at the tropical tropopause (feeding the whole stratosphere through the tropical pipe); stratospheric H_2O production from methane

oxidation; HNO_3 formation from $\text{NO}_2 + \text{OH}$ and heterogeneous reactions on sulfate and PSC aerosols; water vapor and nitric acid loss through permanent dehydration and denitrification of the lower stratosphere produced by PSC gravitational settling; gas emissions from subsonic aviation.

It should be made clear, however, that the mechanisms controlling entry of water into the stratosphere are yet not well understood. Observations suggest that lower stratospheric water vapor has been increasing in the last decade at a rate of about 0.5% per year (Oltmans and Hofmann, 1995), with no significant observed increase of the tropical tropopause temperature (though the data in the tropics are extremely sparse and there are large discrepancies between data sets). Although part of the stratospheric H_2O enhancement may be attributable to increasing methane oxidation or very marginally ($<0.02\%/yr$) to air traffic growth (Danilin et al., 1998), it is realistic to assume that changes in the troposphere-stratosphere exchange of water has taken place. A possibility is that the water vapor increase is due to a change in the location of cross-tropopause transport, which could cause an increased flux to the stratosphere by simply broadening the region of cross-tropopause transport to latitudes slightly further from the equator, but this is still uncertain and speculative. It is then possible that there could be substantially more water in the future stratosphere even if the tropopause temperature has not changed. In addition we have seen in Fig. 10 (and related discussion) that models can differ substantially in their prediction for future changes of the tropopause temperature.

Table 7 summarizes the model calculated changes of stratospheric water vapor and nitric acid for the different 2030 experiments, with respect to 2000. Experiment ‘TS’ is a sensitivity study where we use the 2030-2000 mean zonal temperature changes from the GISS model instead of the interactively calculated ULAQ changes. The globally averaged stratospheric H_2O increase is 3%

in the ‘CH’ simulation, and this is almost completely produced by growing methane oxidation. The water change increases up to 9% in the ‘TC’ simulation and to 20% in the sensitivity case ‘TS’ (as expected by the larger warming of the tropical tropopause in the GISS model, with respect to ULAQ). The net increase of stratospheric nitric acid, on the other hand, is produced by: (a) growing subsonic air-traffic in the upper troposphere ($\Delta\text{HNO}_3 \sim 0.45$ ppbv at 12 km altitude in the northern mid-latitudes) and (b) increasing N_2O in the stratosphere ($\Delta\text{HNO}_3 \sim 1.0$ ppbv at 25 km in the northern mid-latitudes). The decrease from ‘CH’ to ‘TC’ and ‘TS’ is produced by the additional denitrification due to polar cooling and PSC enhancement (see ahead).

The above numbers give us confidence that the large uncertainty in model predictions of water vapor changes will not play a major role in the calculation of future PSCs: IPCC (1999) has in fact shown that a 15% increase of stratospheric H_2O may enhance the surface area density of PSCs by about 20% in the Arctic region. As we will see later in the paper, the lower stratospheric cooling predicted by the ULAQ climate-chemistry model in year 2030 implies a factor of 5 increase of both surface area density and optical depth (averaged between November and March and poleward of 60N). The water vapor distribution, on the other hand, may significantly affect the mid-stratospheric gas phase ozone chemistry via OH production. The ULAQ model has been carefully validated for the stratospheric prediction of temperature (Fig. 13), H_2O (Fig. 14) and HNO_3 (Fig. 15), that is dynamical and chemical fields directly involved in the formation and growth of PSC particles. Dynamical predictions of the ULAQ GCM are close enough to climatological observations, for both mean zonal temperatures and winds, mean meridional circulation and planetary waves (see also Pitari (1993)). Improvements in the parameterization of tropospheric heating has allowed a much better representation of the lower stratosphere, with

respect to Pitari et al. (1992). The Arctic vortex is about 3K warmer than observed (Fig. 13a), while the opposite is found for the Antarctic vortex (Fig. 13c). The GCM, however, does not reproduce a springtime Antarctic ozone hole so pronounced as in the last decade observations, so that September and October polar temperatures are about 2-5 K warmer than observed (Kiehl et al., 1988). For this reason we should expect in the model less PSC formation than in the real atmosphere during the Antarctic spring.

Tropospheric water vapor in the ULAQ-CTM is simply calculated by scaling saturation values with climatological relative humidity, while transport and full chemistry are taken into account above the tropopause. The CTM (Fig. 14) is able to reproduce the observed low values of water vapor above the tropical tropopause (≤ 3 ppmv) up to about 50N (following the isentropic penetration of dry air during the winter months immediately above the tropopause level). The model is also able to reproduce the secondary minimum at the equator near 25 km, which, on the other hand, results from the vertical upward displacement of the previous year tropopause minimum. This is a proof of a rather good isolation of the tropical pipe, along with a realistic equatorial upwelling, although the secondary minimum in the model is about 2 km above the observed position. Deviations with respect to HALOE observations are never larger than $\pm 10\%$ below 30 km altitude and equatorward of $\pm 40^\circ$ latitude. Taking into account the rather crude vertical resolution and the intrinsic difficulty of modeling water vapor immediately above a region of large horizontal and vertical gradients, the ULAQ model reproduces stratospheric water vapor in a reasonable way. The April comparison is particularly interesting in terms of model validation because, while on one side the chemical production from methane oxidation is close to annually averaged conditions, on the other hand it gives the possibility to see how well the rather dry layer between 150 and 200 hPa in the Northern Hemisphere mid-latitudes is captured

by the model. The latter feature would not be visible in annually averaged conditions.

The comparison of model HNO_3 with CLAES observations (Fig. 15) is normally in the ± 1 ppbv range, except below the region of PSC formation and particularly in the Southern Hemisphere. Here the model underestimates nitric acid, pointing out to a too fast denitrification of the lower stratosphere via particle gravitational settling; this is consistent with the colder wintertime polar temperatures shown in Fig. 13c. In addition, as noted in Pitari et al. (1993), the rather crude radial resolution adopted for PSC particles ends up in a size distribution probably shifted toward coarse particles, thus enhancing the denitrification and dehydration sinks. Nice features of the model are the equatorial low values of HNO_3 at 30 km height and the correct accumulation at the high-latitudes with maxima at about 25 km altitude.

Fig. 16 shows the model calculated frequency of PSC occurrence in both polar regions in the baseline simulation of 2000 (top panel) and in the 2030-TC simulation (see Table 1). An important feature is the extension of the time period of PSC formation in both hemispheres, in particular in months with sunlight presence at high latitudes after the polar night. Even more important is the large increase of PSC presence over the Arctic with respect to year 2000 conditions: this polar aerosol enhancement is a consequence of a more stable and colder polar vortex.

A comparison with observations is presented in Fig. 17 for the frequency and in Fig. 18 for the optical depth. The optical depth enhancement in 2030 is due to the increasing loading of both background sulfate (see Table 5) and PSC particles. If we compare the polar optical depth of PSC aerosols alone, a factor of 5 increase is predicted in 2030-TC with respect to 2000 in the Arctic region, averaging between November and March. This large increase in optical depth is also found in surface area density, thus affecting the rates of heterogeneous reactions relevant

for the ozone photochemistry.

The agreement with SAM-II data is rather good, although the model has a tendency to overestimate the Antarctic PSC frequency during July and to underestimate it during September-October. This is even clearer when looking at POAM-II data: as mentioned before, one possible explanation for the model underestimated PSC frequency during the Antarctic spring is that the lower stratospheric cooling produced by the deepening of the ozone hole during 1990's is only partially reproduced in the model. This may also explain the difference between SAM-II and POAM-II frequency data. The frequency overestimation during July may be related to a tendency of the ULAQ model to have a rather zonally symmetric Antarctic polar vortex, with too small longitudinal variability of the temperature field. This ends up increasing the early austral winter probability of PSC occurrence over the whole latitude band of averaging (64S-80S). The longitudinal distribution of PSCs appears to be well represented by the model in the Arctic region, as shown in Fig. 17b.

5 Ozone results

The overall strategy of this work is to carefully validate the model in terms of aerosol prediction, looking at both sulfate and PSC particles, as well as at their precursors (SO_2 , H_2O , HNO_3 and temperature fields). Once we have enough confidence on the model capability to predict future trends of these particles (in the limits of any climate model to predict "realistic" future perturbations of atmospheric dynamics), we can then look at the chemical impact on stratospheric ozone, through heterogeneous chemical reactions. Validation of ULAQ models for ozone profiles and column has been made in NASA (1999), Pitari et al. (2001) and Bregman et al. (2001),

using satellite, ozonesonde and aircraft measurements. The calculated ozone distribution in the stratosphere is typically in a 10-20% level of accuracy. Larger discrepancies (30-40%) are found for the late winter and springtime maxima in the mid-high latitude lowermost stratosphere and upper troposphere, pointing out to an insufficient strat/trop downward flux in the O_3 accumulation region. In addition (as mentioned before), the ULAQ GCM does not catch a springtime Antarctic ozone hole as pronounced as in the observations, although this is typical of the majority of 3D global models with on-line ozone photochemistry.

Future ozone changes, however, result from the action of several simultaneous physico-chemical mechanisms, not simply heterogeneous chemistry; the main feedback processes of future aerosol and climate changes on ozone are discussed here. A comparison is made of future steady-state ozone perturbations related separately to climate and sulfur emission changes in year 2030, that is when the chemically-driven O_3 recovery should take place (WMO, 1999). The purpose is an attempt to quantify the impact of these dynamical and heterogeneous chemical perturbations on the rate of future ozone recovery.

Stratospheric circulation changes in future climate are essentially represented by a reinforcement of the lower stratospheric residual circulation with enhanced upwelling in the tropics (Fig. 19a,b) and stronger subsidence at mid-latitudes (Fig. 19c). The latitudinal gradient of the diabatic heating in the 50-200 hPa layer is enhanced in a GHG richer atmosphere, so that the tropical UT/LS tends to warm up with respect to mid-latitudes through longwave cooling and tropospheric convective heating forced by a warmer surface. Tropospheric temperature changes, in turn, tend to increase the atmospheric stability, so that planetary wave propagation in the stratosphere is altered and polar vortices are found to be more stable, thus enhancing O_3 depletion by PSC activated chlorine and bromine radicals. The net effect on lower stratospheric ozone

depends non-linearly on the combination of two effects: (a) more efficient mid-latitude downwelling motion bringing more ozone towards regions where the O_3 lifetime is normally longer; (b) more efficient lower stratospheric chemical removal in polar regions, due to more stable vortices and prolonged conditions of polar air chemical processing and consequent decrease of the ozone lifetime. The first dynamical effect is actually more complex when considering perturbations of the ozone transport rates by irreversible horizontal eddy mixing.

Fig. 20 summarizes future trends of the ozone profile due to chemical composition changes (panel a, case ‘CH’) and to perturbations of both chemistry and dynamics (panel b, case ‘TC’). Chemistry-driven O_3 changes are the following: (a) tropospheric increase due to positive trends of NO_x , CO and non-methane hydrocarbons surface production (about 8% average increase per decade, to be intended as an upper limit, due to the use of the IPCC-SRES (2000) scenario ‘A2’); (b) lower stratospheric increase (about 2.5% per decade in the 50-200 hPa layer) due to negative trends of CFCs and halons (producing less inorganic Cl/Br), and positive trends of methane with consequent enhancement of free chlorine conversion into HCl; (c) 1.5% to 3% O_3 increase per decade in the 1-5 hPa layer, due to the negative trend of stratospheric Cl_y ; (d) some decrease in the mesosphere because more HO_x is produced by methane oxidation.

Effects of climate changes are visible in Fig. 20b and can be summarized as follows: (a) O_3 decreases in the tropical lower stratosphere because of the additional equatorial upwelling shown in Fig. 19b; (b) the positive trend in the lower stratosphere is now much smaller with respect to the pure chemistry-driven trend, particularly in the Arctic region, due to a more efficient heterogeneous chemical processing on PSC particles (made possible by the enhanced stability of the polar vortex); (c) positive trends in the upper stratosphere are now larger (about 4-6% per decade at 2 hPa) due to the stratospheric cooling and the associated decreased efficiency of

homogeneous catalytic cycles for ozone depletion.

Fig. 21 is a summary of the calculated ozone perturbations in different experiments. When climate changes are taken into account (experiment ‘TC’), the effect on PSCs is such that the future ozone recovery relative to 2000 is significantly reduced (from 4.5% to 3.7%): an increase of PSC aerosols (both in terms of spatial and temporal distributions) is capable of activating more Cl/Br in the presence of sunlight, thus reducing the ozone lifetime in the polar regions. It should be considered, however, that complex non-linear processes take place, with largely compensating positive and negative ozone anomalies. Summarizing, it is possible to say that dynamical changes have the simultaneous effects of increasing ozone (via stronger Brewer-Dobson circulation and less efficient homogeneous chemistry in the mid-upper stratosphere, due to colder temperatures) and decreasing it in the lower stratosphere (more stable and colder vortices, allowing PSCs to last longer and to be present over wider geographical regions). Sulfur emission changes may reduce the global ozone recovery relative to 2000 up to 0.3% (experiment ‘A2’), through the SSA feedback on heterogeneous chemistry.

Qualitatively similar results on the enhancement of polar ozone losses in future climate conditions were found by Pitari et al. (1992) and Shindell et al. (1998). A quantitative comparison of the ozone changes, however, would not be meaningful due to the much simplified approaches used in these two works for what concerns future aerosol trends and their impact on heterogeneous chemistry.

6 Summary and conclusions

In this paper we have tried to quantify the impact of future climate and emission changes on stratospheric aerosols and ozone. A model validation has first been made with SAGE-II, SAM-

II, POAM-II and UARS data for the distributions of sulfate and PSC aerosols and for the concentrations of H_2O and HNO_3 in the stratosphere. The model is successful in simulating both vertical profiles and horizontal distributions of stratospheric aerosols, except for a PSC underestimation during the Antarctic spring, some overestimation of aerosol extinction in the upper troposphere in the subtropical region, and for a too flat latitudinal gradient of aerosol extinction above 25 km. Major findings are that the OCS source of SSA accounts for about 43% of the integrated sulfate aerosol mass above the tropopause, while stratospheric SO_2 oxidation accounts for about 27%; the remaining 30% is upward transported tropospheric sulfate. The major uncertainty of our calculations has to do with the use of a crude representation of the upper tropospheric sulfate aerosol sink due to ice nucleation, and to the validity of the upper tropospheric scavenging parameterization. The tropopause short wave radiative forcing of SSA is found to be -0.126 W/m^2 in 2000 increasing up to -0.186 W/m^2 in 2030-A2 (+48%); this forcing represents about 23% of the total forcing by atmospheric sulfate aerosols. The integrated stratospheric sulfate mass is found to be 0.151 Tg-S in 2000, close to the 0.156 Tg-S deduced from SAGE-II extinction measurements in volcanically quiet years; the predicted upper limit mass increase for 2030 (experiment ‘A2’) is 35% (0.204 Tg-S).

Regional sulfur emission changes are found to be equally important as globally integrated ones: in particular, positive emission trends in the tropics are found to be capable of increasing the SO_2 mixing ratio at the tropical tropopause (via deep convection uplift), thus affecting the whole lower stratosphere. This mechanism may explain why our conclusions should not be considered inconsistent with the SAGE-II finding that no evident trend is present in SSA in the last 15 years, except for transient volcanic disturbances. This is not surprising if we take into account that global anthropogenic sulfur production has declined over Europe and North-America and has increased over Northern China, with relatively small changes in the critical tropical region. Air traffic increased emission of sulfur, on the other hand, can only be significant for surface area density, while in terms of stratospheric sulfate mass (and optical depth) the contribution of the

whole subsonic aircraft fleet is only of the order of few percents (+3% from our calculations).

Another conclusion of this study is that future climate changes are particularly important for the spatial and temporal distributions of PSCs, with large trends in the Arctic regions due to the increased stability of the polar vortex in a GHG richer atmosphere (Shindell et al., 1998). PSC frequency of occurrence, surface area density and optical depth are found to increase in both polar regions; in particular our calculations predict an average increase of PSC surface area density and optical depth by a factor of 5 in the Arctic between November and March, and by more than one order of magnitude at some locations. As the model predicted lower stratospheric cooling is the driving processes for this polar aerosol increase in future climate conditions, it is necessary to keep in mind that the magnitude of the calculated PSC enhancement can be partly model dependent.

The final step in this study is an attempt to quantify the effects of these changes on future ozone trends. Total ozone recovery in 2030 relative to 2000 is found to decrease from +4.5% to +3.7% when taking into account both climate and surface emission changes: effects related to climate changes (perturbed stratospheric circulation, water vapor distribution, PSC frequency, etc.) account for about 2/3 of the calculated slow down of the O₃ recovery rate. Complex non-linear processes are responsible for these ozone changes in future climate conditions (with partly compensating positive and negative anomalies): stronger Brewer-Dobson circulation, less efficient homogeneous chemistry in the mid-upper stratosphere (due to colder temperatures), more stable and colder vortices allowing PSCs to last longer and to be present over wider geographical regions.

Acknowledgements. This work is funded by EU programme TRADE-OFF (EVK2-CT-1999-00030). Part of this work was presented at the European Workshop “ Aviation, Aerosols, Contrails and Cirrus Clouds (A²C³)”, Seeheim, Germany, July 10-12, 2000, (Schumann and Amanatidis, 2001).

References

- Andreae, M.O., The emission of sulfur to the remote atmosphere: background paper, in “The biogeochemical cycling of sulfur and nitrogen in the remote atmosphere”, J.N. Galloway et al. Eds, *NATO-ASI Series C*, 159, 5-25, 1985.
- Bates, T.S., B.K. Lamb, A. Guenther, J. Dignon, and R.E. Stoiber, Sulfur emissions to the atmosphere from natural sources, *J. Atmos. Chem.*, 14, 315-337, 1992.
- Brasseur, G., and S. Solomon, Aeronomy of the middle atmosphere, *D. Reidel Publishing Company*, 1984.
- Bregman, A., M.C. Krol, J. Lelieveld, W.A. Norton, A. Iwi, H. Teyss  re, M. Chipperfield, G. Pitari, and J.K. Sundet, Chemistry-transport model comparison with ozone observations in the mid-latitude lowermost stratosphere, *J. Geophys. Res.*, in press, 2001.
- Carrol, M.A., Measurements of OCS and CS₂ in the free troposphere, *J. Geophys. Res.*, 90, 10483-10486, 1985.
- Danilin, M.Y., et al., Aviation fuel tracer simulation: model intercomparison and implications, *Geophys.Res.Lett.*, 25, 3947-3950, 1998.
- Feichter, J., and P.J. Crutzen, Parameterization of vertical tracer transport due to deep cumulus convection in a global transport model and its evaluation with ²²²Rn measurements, *Tellus*, 42B, 100-117, 1990.
- Feichter, J., E. Kjellstr  m, H. Rodhe, F. Dentener, J. Lelieveld, and G.-J. Roelofs, Simulation of the tropospheric sulfur cycle in a global climate model, *Atmos. Environ.*, 30, 1693-1707, 1996.
- Fromm, M.D., P.M. Bevilacqua, J. Hornstein, E. Shettle, K. Hoppel, and J.D. Lumpe, An analysis of POAM II Arctic polar stratospheric cloud observations: 1993-1996, *J. Geophys. Res.*, 104, 24341-24357, 1999.
- Ganzeveld, L., J. Lelieveld, and G.J. Roelofs, A dry deposition parameterization for sulfur oxides in a chemistry and general circulation model, *J. Geophys. Res.*, 103, 5679-5694, 1998.
- Graf, H.-F., J. Feichter, and B. Langmann, Volcanic sulfur emissions: Estimate of source strength and its contribution to the global sulfate distribution, *J. Geophys. Res.*, 102, 10727-10738, 1997.

- Grant, W.B., E.V. Browell, C.S. Long, L.L. Stowe, R. Grainger, and A. Lambert, Use of volcanic aerosols to study the tropical stratospheric reservoir, *J. Geophys. Res.*, *101*, 3973-3988, 1996.
- Grewe V., D. Brunner, M. Dameris, J.L. Grenfell, R. Hein, D. Shindell, and J. Staehlin, Origin and variability of upper tropospheric nitrogen oxides and ozone at northern mid-latitudes, *Atmos. Environ.*, *35*, 3421-3433, 2001.
- Hamill, P., C.S. Kiang, and R.D. Cadle, The nucleation of H₂SO₄ solution aerosol particles in the stratosphere, *J. Atmos. Sci.*, *34*, 150-162, 1977.
- Hansen, J.E., A. Lacis, R. Ruedy, and M. Sato, Potential climatic impact of Mount Pinatubo eruption, *Geophys. Res. Lett.*, *19*, 215-218, 1992.
- Inn, E.C.Y., J.F. Vedder, B.J. Tyson, and D. O'Hara, COS in the stratosphere, *Geophys. Res. Lett.*, *6*, 191-193, 1979.
- IPCC Special report on aviation and the global atmosphere, J.E. Penner et al. Eds., *Cambridge University Press*, Cambridge, UK, 1999.
- IPCC Special report on emission scenarios, N. Nakicenovic et al. Eds., *Cambridge University Press*, Cambridge, UK, 2000.
- IPCC Third assessment report on climate change, *Cambridge University Press*, Cambridge, UK, in press, 2001.
- Jacob, D.J. and M.J. Prather, Radon-222 as a test of convective transport in a general circulation model, *Tellus*, *42B*, 118-134, 1990.
- JPL, Chemical kinetics and photochemical data for use in stratospheric Modeling, *JPL publ. 97-4*, Pasadena, California, 1997.
- Kent, G.S. and M.P. McCormick, SAGE and SAM II measurements of global stratospheric aerosol optical depth and mass loading, *J. Geophys. Res.*, *89*, 5303-5314, 1984.
- Kent, G.S., D.M. Winker, M.T. Osborn, K.M. Skeens, A model for the separation of cloud and aerosol in SAGE II occultation data, *J. Geophys. Res.*, *98*, 20725-20735, 1993.
- Kent, G.S., C.R. Trepte and P.L. Luckey, Long-term Stratospheric Aerosol and Gas Experiment I and II

- measurements of upper tropospheric aerosol extinction, *J. Geophys. Res.*, *103*, 28863-28874, 1998.
- Kiehl, J.T., B.A. Boville and B.P. Briegleb, Response of a general circulation model to a prescribed Antarctic ozone hole, *Nature*, *332*, 501-504, 1988.
- Larsen, N., Chemical understanding of ozone loss - heterogeneous processes: Microphysical understanding and outstanding issues, *Proceedings of the Fifth European Symposium on Polar Stratospheric Ozone Research*, St. Jean de Luz, France, September 1999, Air Pollution Research Report, European Commission, 2000.
- Langner, J. and H. Rodhe, A global three-dimensional model of the tropospheric sulfur cycle, *J. Atmos. Chem.*, *13*, 225-263, 1991.
- Liu, S.C., J.R. Mc Affee and R.J. Cicerone, Radon-222 and tropospheric vertical transport, *J. Geophys. Res.*, *89*, 7291-7297, 1984.
- Lohmann, U., J. Feichter, C.C. Chuang and J.E. Penner, Prediction of the number of cloud droplets in the ECHAM GCM, *J. Geophys. Res.*, *104*, 9169-9198, 1999.
- McCormick, M.P., P. Hamill, T.J. Pepin, W.P. Chou, T.J. Swisler, and L.R. McMaster, Satellite studies of the stratospheric aerosol, *Bull. Amer. Meteorol. Soc.*, *60*, 1038-1046, 1979.
- McCormick, M.P., and P.H. Wang, Satellite measurements of stratospheric aerosols, in "Transport processes in the middle atmosphere", G.Visconti and R. Garcia Eds., *NATO-ASI Series C*, *213*, 103-120, 1987.
- Muller, J.-F., and G. Brasseur, A three-dimensional transport model of the global troposphere, *J. Geophys. Res.*, *100*, 16445-16490, 1995.
- NASA, Models and measurements intercomparison II, J.H. Park et al. Eds., *NASA/TM-1999-209554*, 494, 1999.
- Oort, A.H., Global atmospheric circulation statistics, 1958-1973. *NOAA professional paper 14*, U.S. Department of Commerce, Washington DC, 1983.
- Oltmans, S.J., and D.J. Hofmann, Increase in lower-stratospheric water at mid-latitude Northern Hemisphere site from 1981 to 1994. *Nature*, *374*, 146-149, 1995.

- Pinto, J.P., R.P. Turco, and O.B. Toon, Self limiting physical and chemical effects in volcanic eruption clouds, *J. Geophys. Res.*, *94*, 11165-11174 1989.
- Pitari, G., S. Palmeri, G. Visconti, and R.G. Prinn, Ozone response to a CO₂ doubling: Results from a stratospheric circulation model with heterogeneous chemistry, *J. Geophys. Res.*, *97*, 5953-5962, 1992.
- Pitari G., A numerical study of the possible perturbation of stratospheric dynamics due to Pinatubo aerosols: Implications for tracer transport, *J. Atmos. Sci.*, *50*, 2443-2461, 1993.
- Pitari, G., V. Rizi, L. Ricciardulli, and G. Visconti, High-speed civil transport impact: Role of sulfate, nitric acid trihydrate, and ice aerosol studied with a two-dimensional model including aerosol physics, *J. Geophys. Res.*, *98*, 23141-23164, 1993.
- Pitari, G., E. Mancini, A. Bregman, H.L. Rogers, J.K. Sundet, V. Grewe, and O. Dessens, Sulphate particles from subsonic aviation: Impact on upper tropospheric and lower stratospheric ozone, *Phys. Chem. of Earth*, *26C*, in press, 2001.
- Prather M.J., Catastrophic loss of stratospheric ozone in dense volcanic clouds, *J. Geophys. Res.*, *97*, 10187-10191, 1992.
- Randel, W. J., Global Atmospheric circulation statistic, 1000-1 mb, *NCAR/TN-366*, NCAR, Boulder, Colorado, 1992.
- Randel, W. J., F. Wu, J. M. Russell III, J.W. Waters, and L.Froidevaux, Ozone and temperature changes in the stratosphere following the eruption of Mount Pinatubo, *J. Geophys. Res.*, *100*, 16753-16764, 1995.
- Ricciardulli, L., G. Pitari, and G. Visconti, Two-dimensional modeling of the time evolution of the Pinatubo aerosol cloud, in "The Mount Pinatubo eruption effects on the atmosphere and climate", G. Fiocco et al. Eds., *NATO-ASI Series, I 42*, 1996.
- Rodhe H., The transport of sulfur and nitrogen through the remote atmosphere: background paper in "The biogeochemical cycling of sulfur and nitrogen in the remote atmosphere", J.N. Galloway et al. Eds, *NATO-ASI Series C, 159*, 105-124, 1985.
- Rossow, W.B., B.L. Garder, P.J. Lu, and A.W. Walker, Satellite Cloud Climatology Project (ISCCP),

- documentation on cloud data, *WMO/TD-266*, WMO, Geneva, 78, 1987.
- Schumann, U. and G.T. Amanatidis (Eds.), Aviation, Aerosols, Contrails and Cirrus Clouds (A²C³), Proceedings of a European Workshop, Seeheim, Germany, July 10-12, 2000, *Air Pollution Research Report 74, EUR 19428*, European Commission, Brussels, pp.314, 2001.
- Shea, D.J., Climatological atlas: 1950-1979, *NCAR/TN-269+STR*, NCAR, Boulder, Colorado, 1986.
- Shindell, D.T., D. Rind, and P. Lonergan, Increased polar stratospheric ozone losses and delayed eventual recovery owing to increasing greenhouse-gas concentrations, *Nature*, *392*, 589-592, 1998.
- Shindell, D.T., R.L. Miller, G.A. Schmidt, and L. Pandolfo, Simulation of recent northern winter climate trends by greenhouse-gas forcing, *Nature*, *399*, 452-455, 1999.
- Shindell, D. T., G. A. Schmidt, R. L. Miller, and D. Rind, Northern Hemisphere winter climate response to greenhouse gas, volcanic, ozone and solar forcing, *J. Geophys. Res.*, *106*, 7193-7210, 2001.
- Spiro, P.A., D.J. Jacob, and J.A. Logan, Global inventory of sulfur emissions with $1^{\circ} \times 1^{\circ}$ resolution, *J. Geophys. Res.*, *97*, 6023-6036, 1992.
- Steel, H.M., and P. Hamill, Effects of temperature and humidity on the growth and optical properties of sulphuric acid-water droplets in the stratosphere, *J. Aerosol. Sci.*, *12*, 517-528, 1981.
- Thomason, L.W., L.R. Poole, and T. Deshler, A global climatology of stratospheric aerosol surface area density from Stratospheric Aerosol and Gas Experiment II measurements: 1984-1994, *J. Geophys. Res.*, *102*, 8967-8976, 1997.
- Turco, R. P., P. Hamill, O.B. Toon, R. C. Whitten, and C.S. Kiang, A one dimensional model describing aerosol formation and evolution in the stratosphere: I. Physical processes and mathematical analogs. *J. Atmos. Sci.*, *36*, 669-717, 1979.
- Turco, R. P., Upper-Atmosphere aerosols: properties and natural cycles, in "The Atmospheric Effects of Stratospheric Aircraft: A first Program Report", *NASA Ref. Publ. 1272*, pp. 65-91, 1992.
- Turco, R. P., J.-X. Zhao, and F. Yu, A new source of tropospheric aerosols: ion-ion recombination, *Geophys. Res. Lett.*, *25*, 635-638, 1998.
- Yue, G.K., L.R. Poole, P.H. Wang, and E.W. Chiou, Stratospheric aerosol acidity, density, and refractive

- index deduced from SAGE-II and NMC temperature data, *J. Geophys. Res.*, *99*, 3727-3738, 1994.
- Weisenstein, D., G.K. Yue, M.K.W. Ko, N.-D. Sze, J.M. Rodriguez, and C.J. Scott, A two-dimensional model of sulfur species and aerosols, *J. Geophys. Res.*, *102*, 13019-13035, 1997.
- WMO, Scientific assessment of ozone depletion: 1991, *Rep. 25*, Geneva, 1992.
- WMO, Scientific assessment of ozone depletion: 1998, *Rep. 44*, Geneva, 1999.

Tables

Table 1. List of numerical experiments.

Experiment	Description
2000-Base	Chemistry boundary conditions for 2000 as in WMO (1999), IPCC-TAR (2001); aerosol and sulfur fluxes as in IPCC-TAR (2001)
2000-NA	No subsonic aircraft
2000-OCS	Only OCS as sulfate precursor
2000-TRP	Sulfate photochemical production only in troposphere
2030-CH	Chemistry boundary conditions for 2030, as in WMO (1999) and IPCC-TAR (2001) (scenario A2); aerosol and sulfur fluxes as in 2000-Baseline
2030-B1	Anthropogenic SO ₂ surface fluxes as in scenario B1 of IPCC-SRES (2000)
2030-A2	Anthropogenic SO ₂ surface fluxes as in scenario A2 of IPCC-SRES (2000)
2030-TC	As in 2030-A2, including temperature and dynamical changes for year 2030
2030-TS	As above, but with mean zonal temperature changes from the GISS model (Shindell et al., 1999)

Table 2. Annual mean sulfate wet deposition fluxes (mg-S/m²/yr).

	Total	Anthropogenic	Natural	Observations
Europe	730	685	45	1000
N. America	370	346	24	340
Oceanic (30S-30N)	90	45	45	87

Table 3. Annual mean optical depth ($\lambda = 1.02 \mu\text{m}$).

Latitude band	Optical depth ($\times 10^{-4}$)							
	SAGE II				CTM			
	10-15 km	15-20 km	20-25 km	25-30 km	10-15 km	15-20 km	20-25 km	25-30 km
80N-60N	18.2	9.5	1.2	0.18	16.5	8.6	2.2	0.55
60N-40N	16.0	10.0	3.0	0.46	18.8	10.0	3.9	0.75
40N-20N	10.1	9.3	4.9	1.00	20.7	11.3	5.2	1.0
20N-EQT	8.7	9.5	8.6	2.40	16.0	11.8	6.8	1.93
EQT-20S	8.4	10.5	9.6	2.70	8.1	8.6	6.6	2.64
20S-40S	10.6	12.2	6.0	1.20	8.8	9.5	5.2	1.23
40S-60S	17.0	13.2	3.6	0.60	14.7	8.9	3.9	0.85
60S-80S	18.9	9.5	1.0	0.20	16.2	8.0	2.3	0.76

Table 4. Global sulfur budget.

Model	Sulfur	Precurs.	Gas.	Aqu.	SO ₂	SO ₂	SO ₄ ⁼	SO ₄ ⁼	SO ₄ ⁼	SO ₄ ⁼	P
	source	Dep.	Oxid.	Oxid.	Burden	Lifetime	dry dep.	wet dep.	Burden	Lifetime	
	Tg-S/yr	%	%	%	Tg-S	days	%	%	Tg-S	days	
CTM	110	41	13	46	0.55	2.1	9	91	0.81	4.7	2.6
COSAM (Average)	98.6	45	12	43	0.40	1.6	16	84	0.70	4.5	2.6
COSAM (S.D.)	12	13	5	17	0.13	0.6	7	7	0.19	1.1	0.8

Table 5. Stratospheric sulfate aerosol budget and tropopause short wave radiative forcing.

	Natural flux (Tg-S/yr)	Anthr. flux (Tg-S/yr)	SO ₂ (Tg-S)	SO ₄ ⁻ (Tg-S)	Aerosol (Tg)	τ - 1.02 μm ($\times 10^{-4}$)	Forcing (W/m ²)
SAGE-II				0.156	0.720	15.0	
2000	41	69	25.7	0.151	0.697	14.8	-0.126
2000-NA	41	69	23.0	0.147	0.677	14.4	-0.123
2000-OCS	($\chi_{OCS}=500$ ppt)	0	5.7	0.065	0.262	5.7	-0.048
2000-TRP	41	69		0.046	0.255	5.4	-0.046
2030-CH	41	69	33.2	0.160	0.746	15.9	-0.135
2030-B1	41	53.5	31.5	0.162	0.752	16.4	-0.140
2030-A2	41	112	40.0	0.204	0.968	21.9	-0.186
2030-TC	41	112	37.0	0.196	0.946	21.0	-0.179

Table 6. Stratosphere-troposphere sulfate budget.

	SO ₄ ⁻ mass (Tg-S)	SO ₄ ⁻ mean load (mg/m ²)	Aerosol mass (Tg)	Aerosol mean load (mg/m ²)	τ 0.55 μm ($\times 10^{-4}$)	K _e 0.55 μm (m ² g ⁻¹)	K _e 1.02 μm (m ² g ⁻¹)	ΔF short wave (Wm ⁻²)
Strat.	0.15	0.90	0.70	1.37	42	3.06	1.08	-0.125
Trop.	0.78	4.70	6.70	13.1	530	4.05	1.90	-0.425
Strat./Total								
(%)	16	16	10	10	7.5			23

Table 7. Annually and globally averaged percent changes of stratospheric H₂O and HNO₃ (2030-2000).

Experiment	$\Delta\text{H}_2\text{O}$ (%)	ΔHNO_3 (%)
2030-CH	3.1	10.7
2030-TC	9.2	4.1
2030-TS	20.4	2.0

Figure Captions

Fig. 1. Annually and zonally averaged mixing ratios of SO_2 (top panel, a) and SO_4^- (bottom panel, b). Units are $\log_{10}(\text{ppbv})$ in (a) and ppbv in (b). Contour line spacing is 0.03 ppbv in panel (b), while 5 isolines per decade are shown in (a).

Fig. 2. Top panels (a, b) show annually averaged SO_2 vertical profiles (ppbv) at the equator (left, a) and at 45N (right, b): solid/dashed lines are for calculations with/without deep convection parameterization, respectively; independent (sparse) measurement ranges are shown in panel (b) for mid-latitude SO_2 (see Langner and Rodhe (1991)). Bottom panels (c, d) show Rn-222 vertical profiles in pCi/SCM for April conditions in a tropical continental site (3S, 60W) (left, c), and for average summertime conditions at continental mid-latitudes (35N-55N). Solid/dashed lines are model calculations with/without convection, respectively; triangles and plus signs in (c) show the results of an independent model calculation (Feichter and Crutzen, 1990), while asterisks in (d) are climatological data from Liu et al. (1984).

Fig. 3. CTM calculations (solid lines) and SAGE-II measurements (asterisks) of aerosol extinction at $\lambda = 1.02 \mu\text{m}$ in the Northern Hemisphere. Units are 10^{-4} km^{-1} . Top/bottom 4 panels (a-d, e-h) are for January and April, respectively. Each block of 4 panels shows the aerosol extinction at 65N (top left: a, e), 45N (top right: b, f), 25N (bottom left: c, g), 5N (bottom right: d, h). SAGE-II measurements are averaged over volcanically quiet years (see text).

Fig. 4. CTM calculations (solid lines) and SAGE-II measurements (asterisks) of aerosol extinction at $\lambda = 1.02 \mu\text{m}$ at 45S latitude. Units are 10^{-4} km^{-1} . Top left panel (a) is for January, top right (b) for April, bottom left (c) for July, bottom right (d) for October. SAGE-II measurements are averaged over volcanically quiet years (see text).

Fig. 5. Annually and zonally averaged fields of surface area density (in units of 10^{-8} cm^{-1} , contour line spacing 0.2). Top/bottom panels (a,b) are for SAGE-II derived value and CTM calculations, respectively. SAGE-II data are averaged over volcanically quiet years. CTM values are obtained as described in the text.

Fig. 6. CTM calculations (solid lines) and SAGE-II derived values (asterisks) of sulfate aerosol surface area density at 45N (top panels: a, b) and 45S (bottom panels: c, d). Left panels (a, c) are for January, right panels (b, d) for April. Units are 10^{-8} cm^{-1} . SAGE-II derived values are averaged over volcanically quiet years. CTM values are obtained as described in the text.

Fig. 7. Zonally averaged total sulfur fluxes (natural + anthropogenic) for 2000 (solid line), 2030 upper limit scenario ‘A2’ (dashed line), 2030 lower limit scenario ‘B1’ (dotted line) (IPCC-SRES, 2000). Units are $\text{kg-S km}^{-2} \text{ yr}^{-1}$.

Fig. 8. Total sulfur flux (natural + anthropogenic) for 2000 (top panel, a) and 2030 (bottom panel, b) (IPCC-SRES, 2000). Data for 2030 refer to the upper limit ‘A2’ scenario. Units are $\text{kg-S km}^{-2} \text{ yr}^{-1}$.

Fig. 9. Annually and zonally averaged changes of surface area density (top panel, a) and mass density (bottom panel, b) of sulfate aerosols. Changes are calculated for case 2030-A2 with respect to the 2000 baseline simulation. Units are $\mu\text{m}^2/\text{cm}^3$ in (a) and ng/m^3 in (b). Three isolines per decade are shown in both panels.

Fig. 10. Monthly and zonally averaged temperature changes (2030-2000) for March, from the ULAQ model (top panel, a) and from the GISS model (Shindell et al., 1999) (bottom panel, b). Units are K; contour line spacing is 0.5 K.

Fig. 11. January averages of the Northern Hemisphere temperature fields (K) at 20 km, for 2000 (top panel, a) and 2030-TC (bottom panel, b).

Fig. 12. Calculated Northern Hemisphere anomalies (2030-2000) of the amplitude of geopotential wavenumber 1 (left) and 2 (right) averaged over December, January, and February winter months (gpm). Solid/dashed lines are positive/negative values, respectively. Contour line spacing is 10 gpm.

Fig. 13. Monthly and zonally averaged temperatures (K), for January (top panels a, b) and July (bottom panels c, d). Panels (a, c) show the ULAQ-GCM predictions (2000); panels (b, d) show data from the National Meteorological Center (NMC) climatology (1979 to 1995) (update of Randel, 1992). The contour line step is 0.5 K.

Fig. 14. April 1992 zonal average of H_2O mixing ratios (ppmv). Top panel (a) is for CTM results using a circulation appropriate for 1992 (Pitari, 1993); bottom panel (b) is for HALOE measurements averaged over April 1992 (NASA, 1999). Contour line step is 0.2 ppmv.

Fig. 15. March 1993 zonal average of HNO_3 mixing ratios (ppbv). Top panel (a) is for CTM results using a circulation appropriate for 1993 (Pitari, 1993); bottom panel (b) is for CLAES measurements averaged over March 1993 (NASA, 1999). Contour line step is 0.5 ppbv.

Fig. 16. Time series of calculated PSC frequency of occurrence in Arctic (NDJFMA) and Antarctic regions (MJJASO). Top panel (a) is for 2000, bottom panel (b) for 2030-TC simulation. Values are averaged between 64 and 80 latitude, that is the same band covered by SAM II observations (WMO, 1992). Contour line step is 0.05.

Fig. 17. Top panel (a): time series of PSC frequency of occurrence at 20 km altitude for both Arctic (NDJFMA) and Antarctic regions (MJJASO). Solid line is for present time conditions (2000), dashed line for 2030-TC simulation, dotted line for 1979-89 SAM-II observations (WMO, 1992), dash-dotted line for POAM-II observations (WMO, 1999). Bottom panel (b): NDJFM averaged PSC frequency at 65N latitude in the 15-25 km altitude layer, as a function of longitude. Solid and dashed

lines are for 2000 and 2030-TC simulations, respectively, dash-dotted line for POAM-II observations (<http://opt.nrl.navy.mil/POAM/>; Fromm et al., 1999).

Fig. 18. Time series of $1.02 \mu\text{m}$ polar stratospheric optical depth in the 64-80 latitude band and calculated from 2 km above the tropopause. Top panel (a) is for both Arctic (NDJFMA) and Antarctic regions (MJJASO), center panel (b) is for the Arctic, bottom panel (c) for the Antarctic region. Solid lines are for present time conditions (2000), dashed lines for 2030-TC simulation, dotted lines for 1979 SAM-II observations (McCormick and Wang, 1987).

Fig. 19. Mean annual residual vertical velocity (\bar{w}^*) averaged between 15N and 15S (top left panel, a). Solid line is for 2000, dashed line for 2030 (experiment ‘TC’). Units are mm/s. Top right panel (b) is an inset of (a) in the lower stratosphere (15-30 km altitude). Bottom panel (c) shows the calculated vertical ozone mass fluxes at 100 hPa for 2000 and 2030-TC (solid and dashed lines, respectively) keeping the ozone field fixed to year 2000 conditions. Units are $10^{-6} \text{ g m}^{-2} \text{ s}^{-1}$.

Fig. 20. Calculated zonally and annually averaged ozone profile change for year 2030 with respect to 2000: top panel (a) is for experiment ‘CH’ (i.e. updated chemistry, fixed SO_2 surface fluxes, fixed climate); bottom panel (b) is for experiment ‘TC’ (i.e. updated chemistry, SO_2 fluxes and climate). Contour line spacing is 2%.

Fig. 21. Calculated steady-state total ozone column percent changes (90S-90N global annual mean) in the different future scenarios for 2030-2000 (left panel, a) and for 2030 with respect to ‘CH’ case (i.e. chemistry update alone) (right panel, b). See Table 1 for a description of the numerical experiments.

Figures

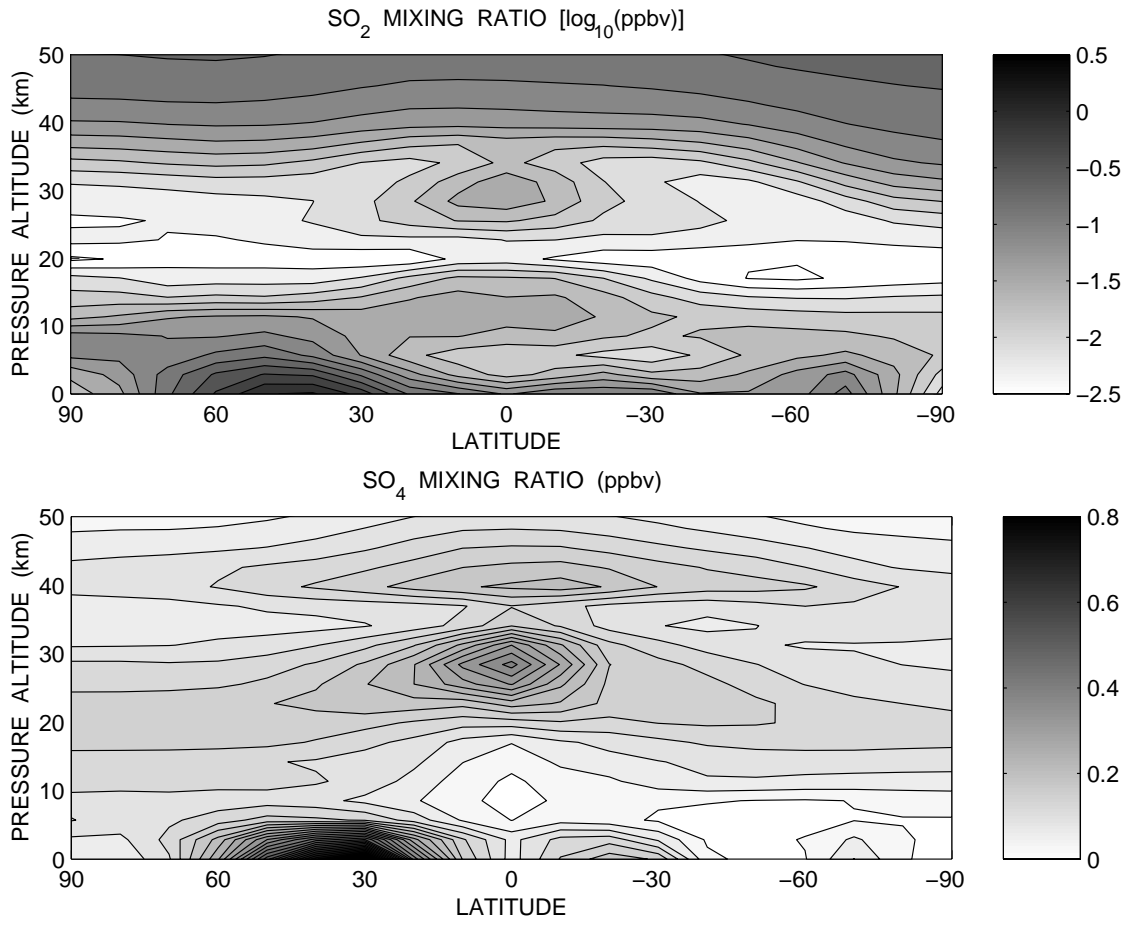


Fig. 1. Annually and zonally averaged mixing ratios of SO_2 (top panel, a) and SO_4^- (bottom panel, b). Units are $\log_{10}(\text{ppbv})$ in (a) and ppbv in (b). Contour line spacing is 0.03 ppbv in panel (b), while 5 isolines per decade are shown in (a).

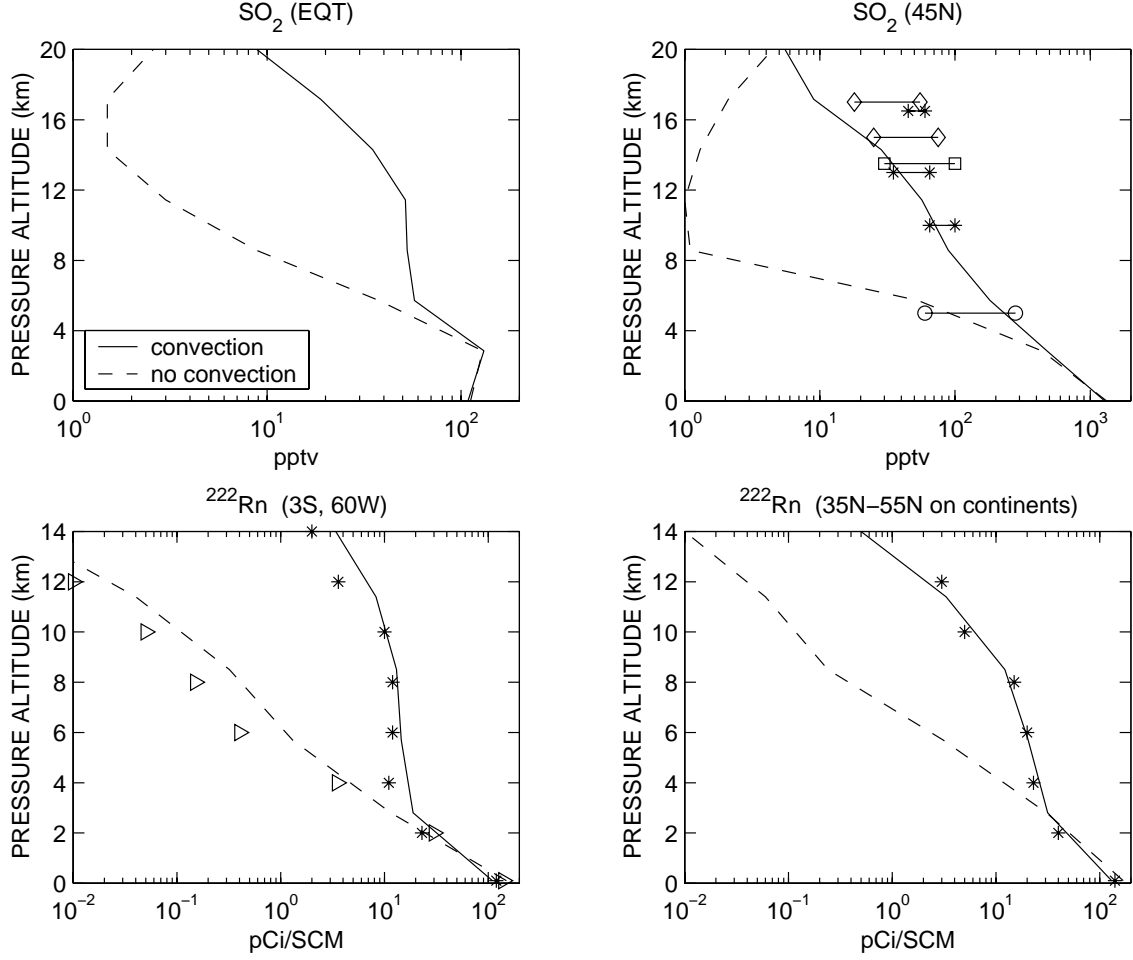


Fig. 2. Top panels (a, b) show annually averaged SO_2 vertical profiles (ppbv) at the equator (left, a) and at 45N (right, b): solid/dashed lines are for calculations with/without deep convection parameterization, respectively; independent (sparse) measurement ranges are shown in panel (b) for mid-latitude SO_2 (see Langner and Rodhe (1991)). Bottom panels (c, d) show Rn-222 vertical profiles in pCi/SCM for April conditions in a tropical continental site (3S, 60W) (left, c), and for average summertime conditions at continental mid-latitudes (35N–55N). Solid/dashed lines are model calculations with/without convection, respectively; triangles and plus signs in (c) show the results of an independent model calculation (Feichter and Crutzen, 1990), while asterisks in (d) are climatological data from Liu et al. (1984).

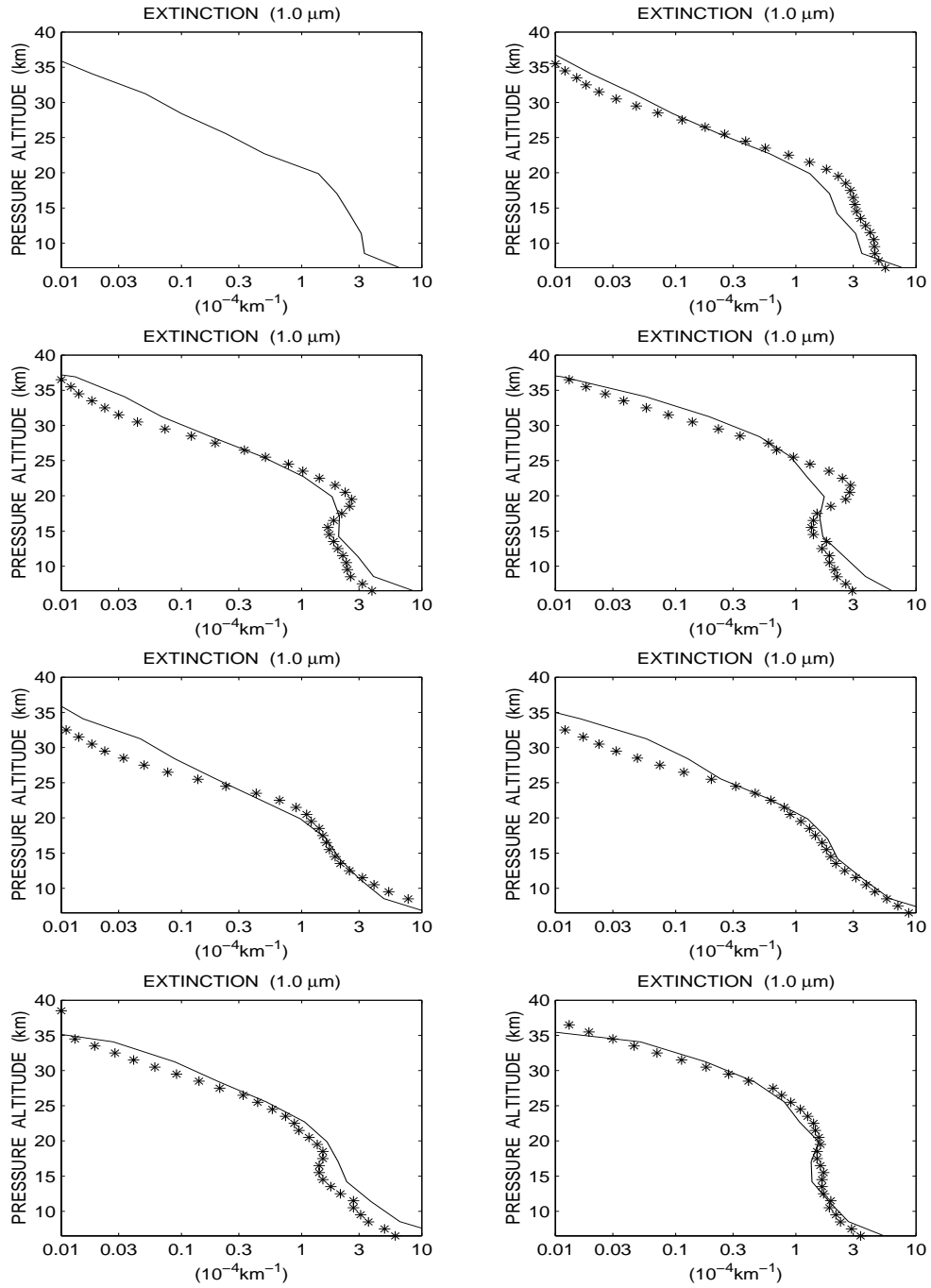


Fig. 3. CTM calculations (solid lines) and SAGE-II measurements (asterisks) of aerosol extinction at $\lambda = 1.02 \mu\text{m}$ in the Northern Hemisphere. Units are 10^{-4} km^{-1} . Top/bottom 4 panels (a-d, e-h) are for January and April, respectively. Each block of 4 panels shows the aerosol extinction at 65N (top left: a, e), 45N (top right: b, f), 25N (bottom left: c, g), 5N (bottom right: d, h). SAGE-II measurements are averaged over volcanically quiet years (see text).

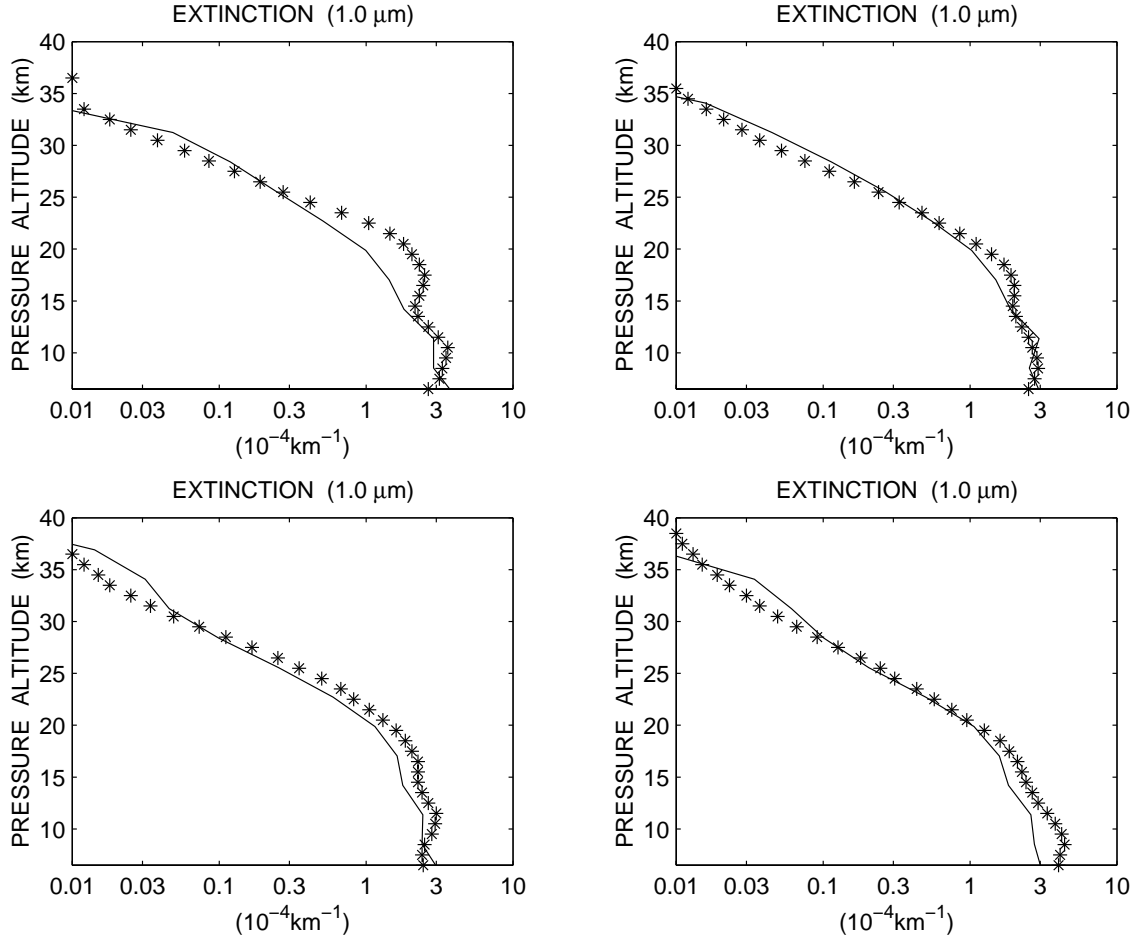


Fig. 4. CTM calculations (solid lines) and SAGE-II measurements (asterisks) of aerosol extinction at $\lambda = 1.02 \mu\text{m}$ at 45S latitude. Units are 10^{-4}km^{-1} . Top left panel (a) is for January, top right (b) for April, bottom left (c) for July, bottom right (d) for October. SAGE-II measurements are averaged over volcanically quiet years (see text).

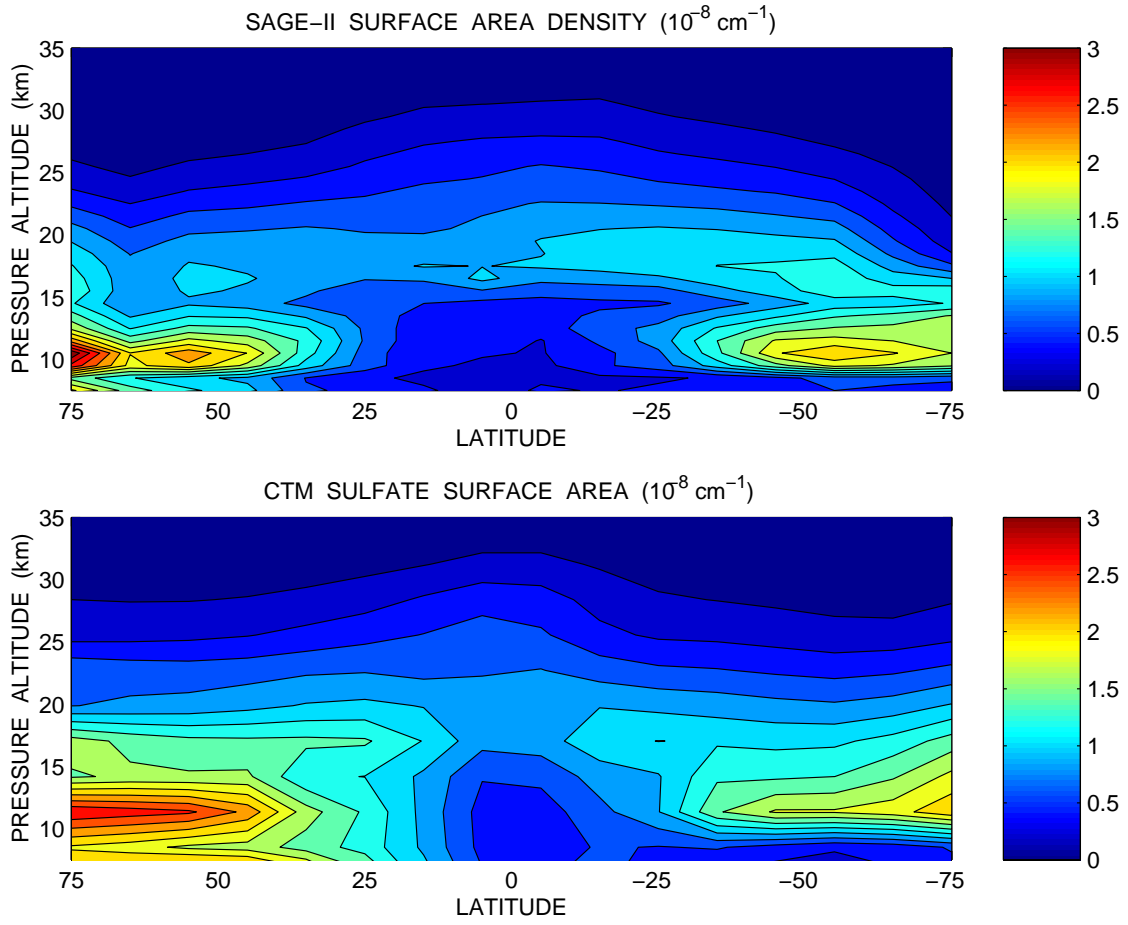


Fig. 5. Annually and zonally averaged fields of surface area density (in units of 10^{-8} cm^{-1} , contour line spacing 0.2). Top/bottom panels (a,b) are for SAGE-II derived value and CTM calculations, respectively. SAGE-II data are averaged over volcanically quiet years. CTM values are obtained as described in the text.

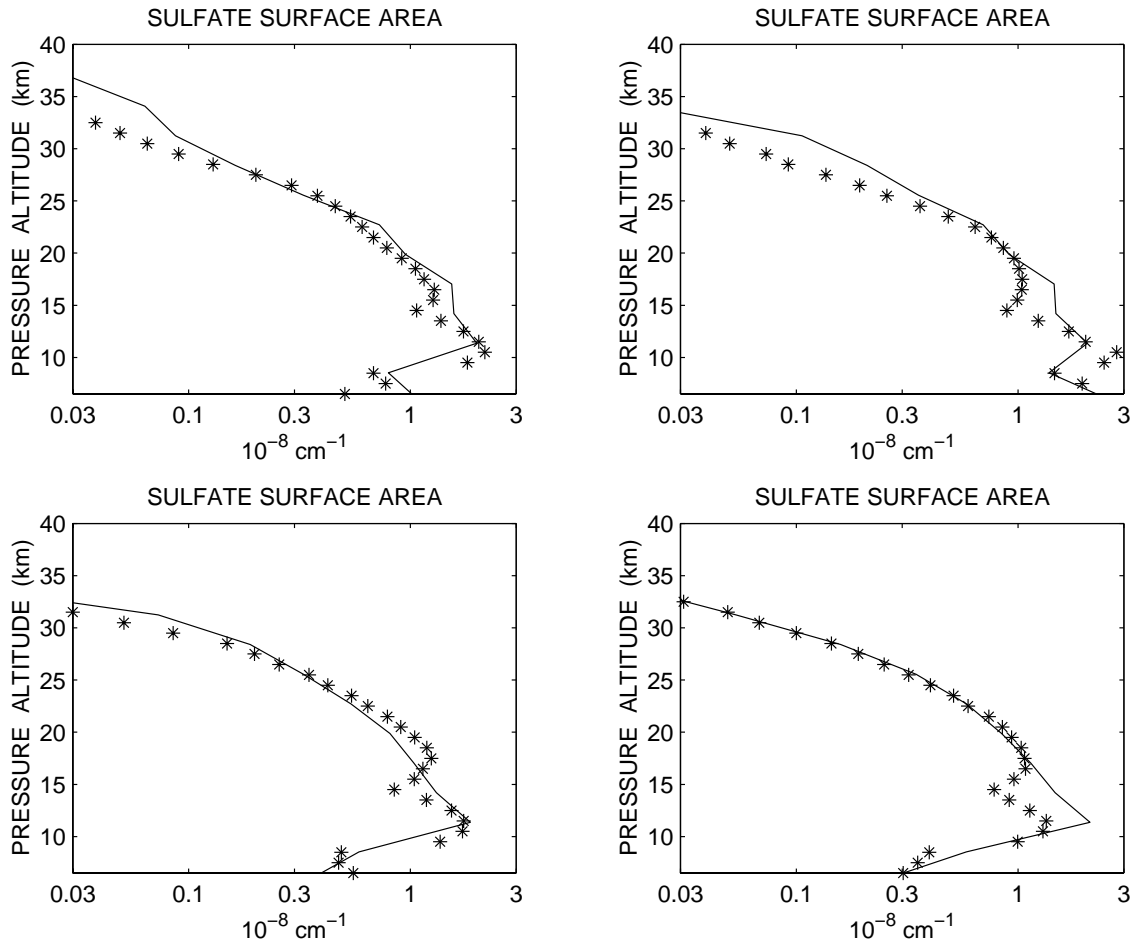


Fig. 6. CTM calculations (solid lines) and SAGE-II derived values (asterisks) of sulfate aerosol surface area density at 45N (top panels: a, b) and 45S (bottom panels: c, d). Left panels (a, c) are for January, right panels (b, d) for April. Units are 10^{-8} cm^{-1} . SAGE-II derived values are averaged over volcanically quiet years. CTM values are obtained as described in the text.

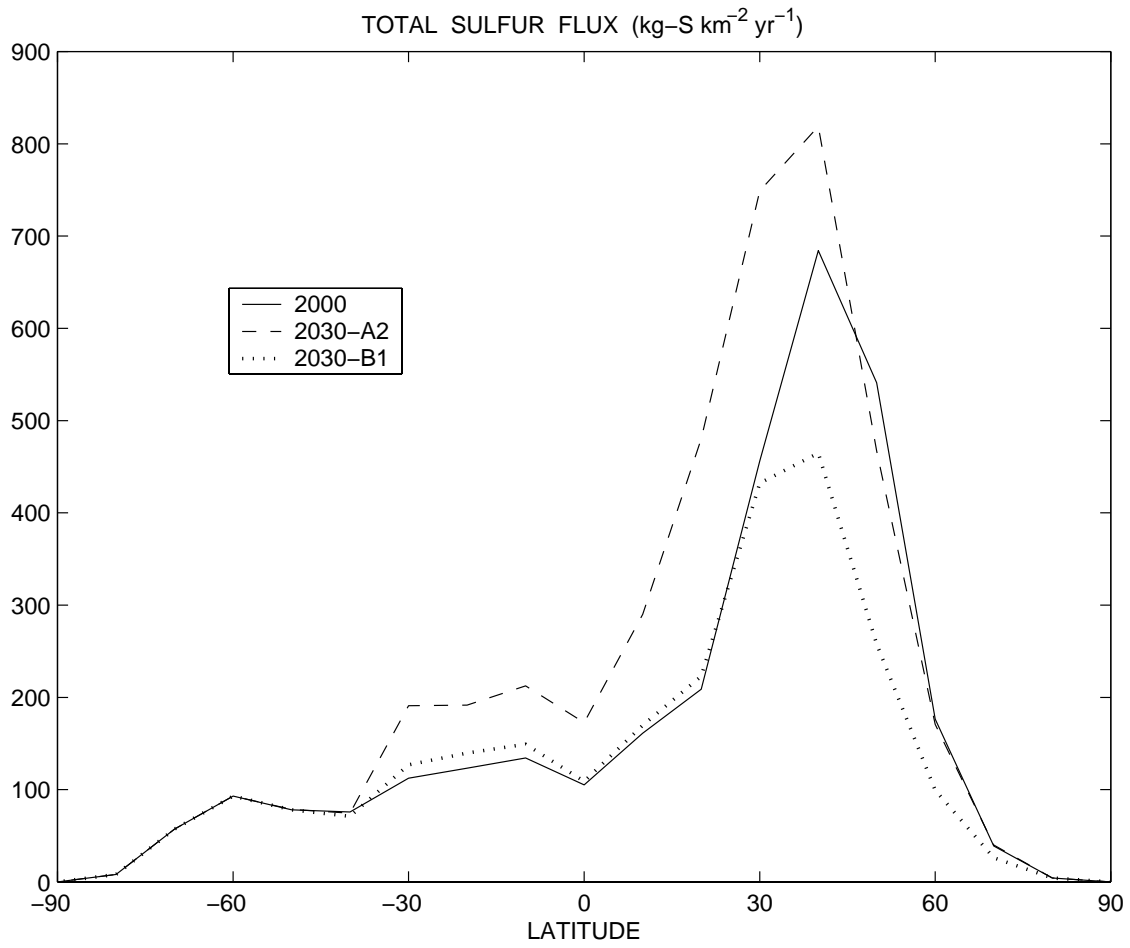


Fig. 7. Zonally averaged total sulfur fluxes (natural + anthropogenic) for 2000 (solid line), 2030 upper limit scenario ‘A2’ (dashed line), 2030 lower limit scenario ‘B1’ (dotted line) (IPCC-SRES, 2000). Units are $\text{kg-S km}^{-2} \text{ yr}^{-1}$.

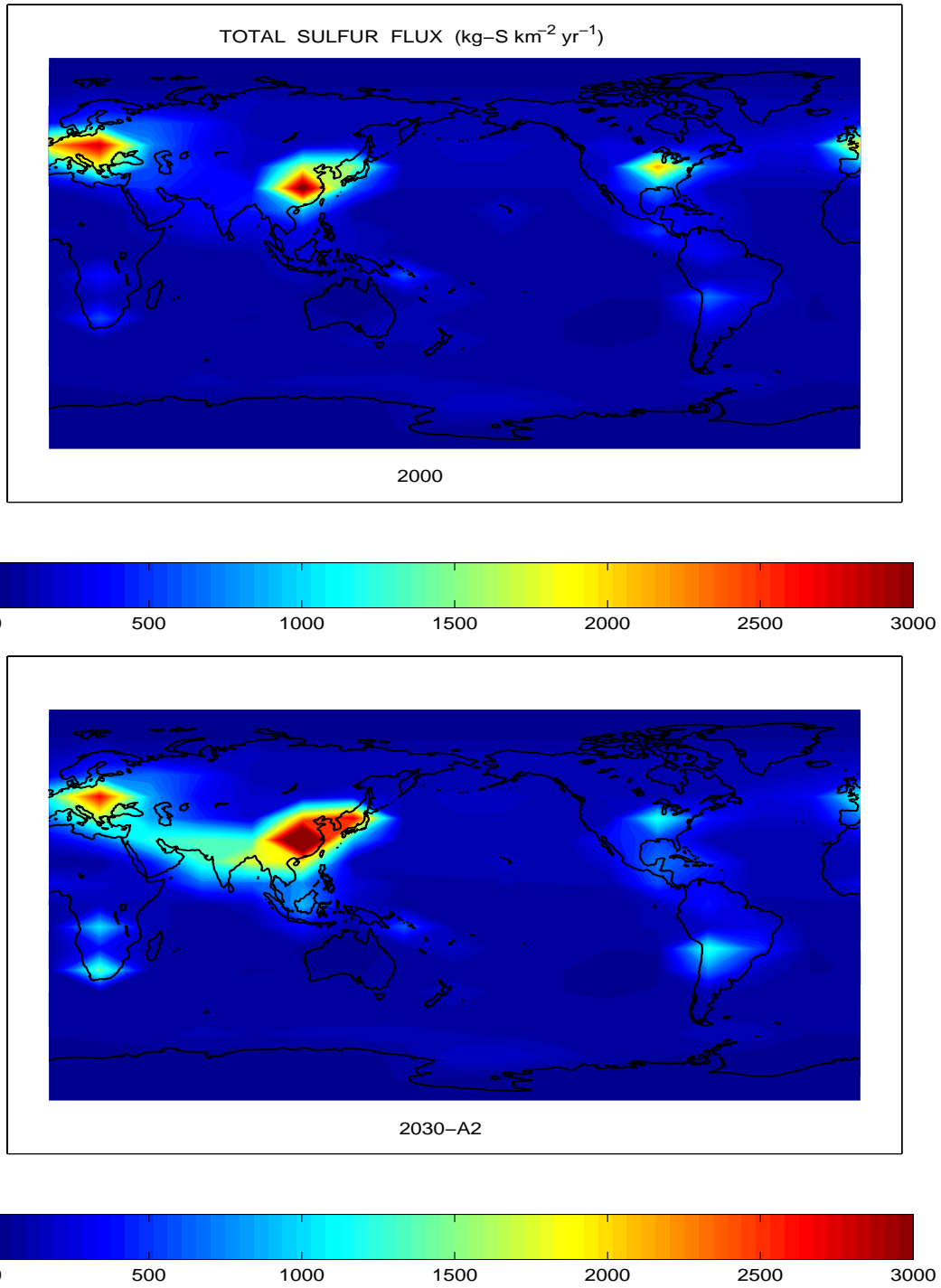


Fig. 8. Total sulfur flux (natural + anthropogenic) for 2000 (top panel, a) and 2030 (bottom panel, b) (IPCC-SRES, 2000). Data for 2030 refer to the upper limit ‘A2’ scenario. Units are $\text{kg-S km}^{-2} \text{yr}^{-1}$.

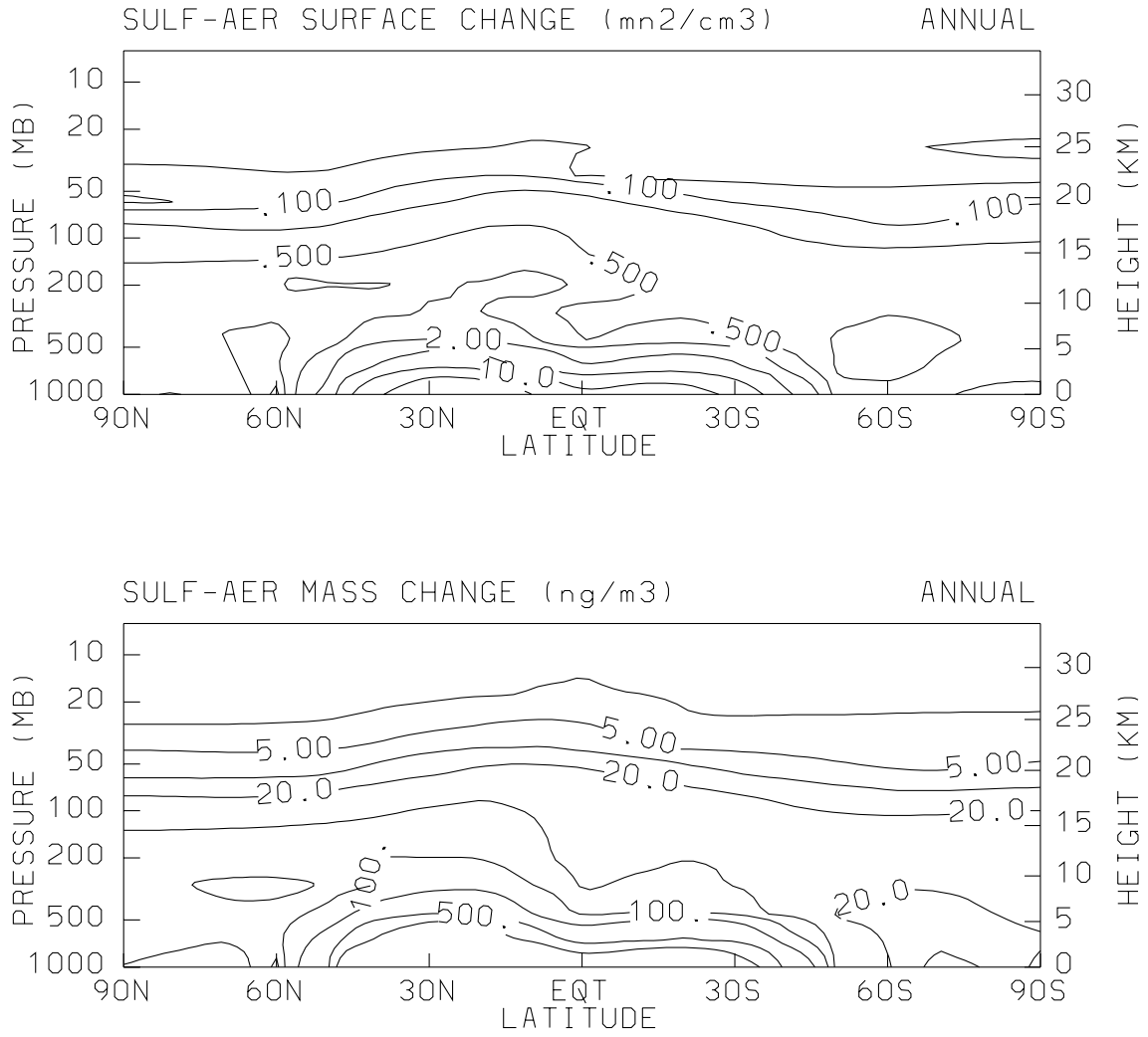


Fig. 9. Annually and zonally averaged changes of surface area density (top panel, a) and mass density (bottom panel, b) of sulfate aerosols. Changes are calculated for case 2030-A2 with respect to the 2000 baseline simulation. Units are $\mu\text{m}^2/\text{cm}^3$ in (a) and ng/m^3 in (b). Three isolines per decade are shown in both panels.

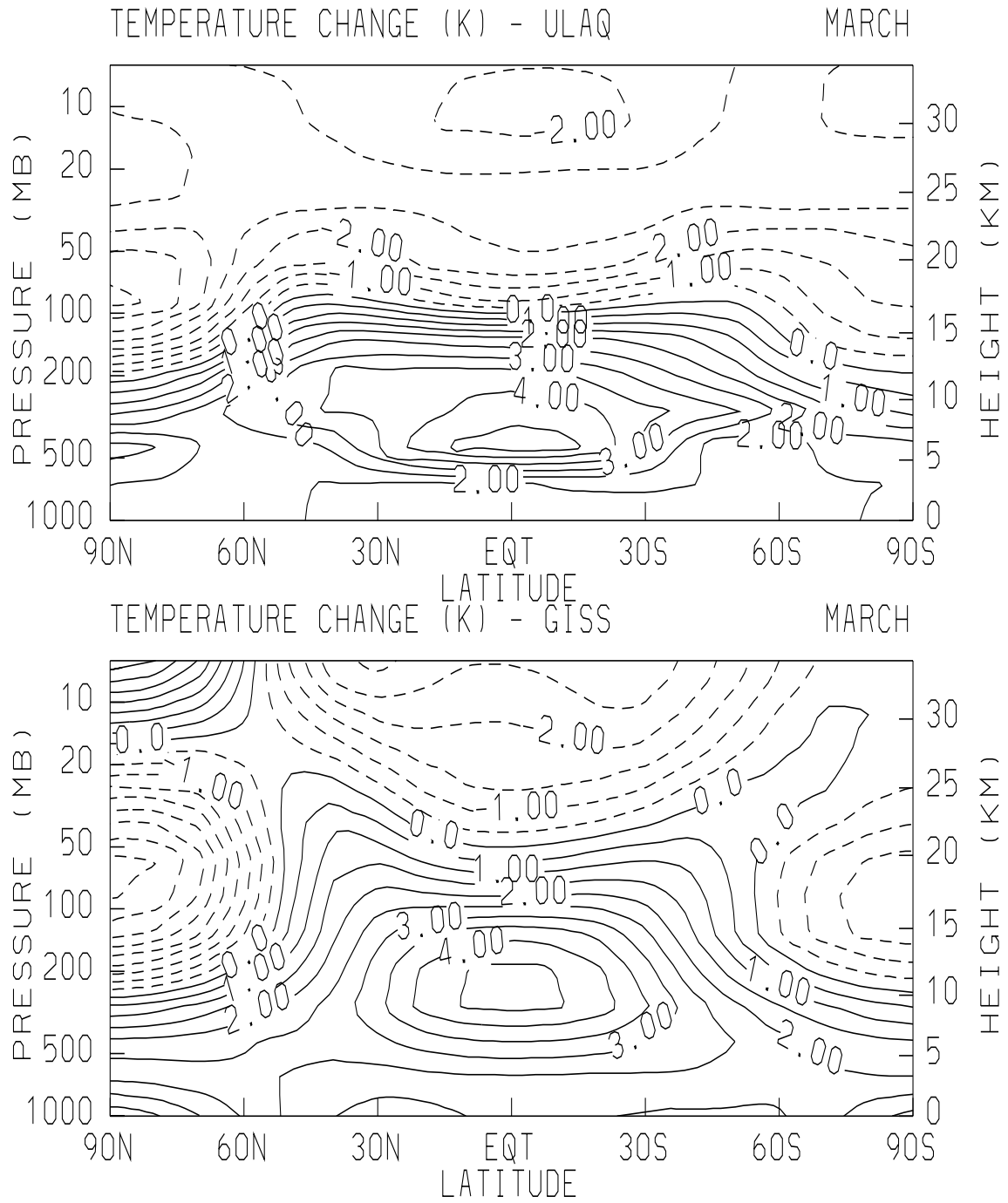


Fig. 10. Monthly and zonally averaged temperature changes (2030-2000) for March, from the ULAQ model (top panel, a) and from the GISS model (Shindell et al., 1999) (bottom panel, b). Units are K; contour line spacing is 0.5 K.

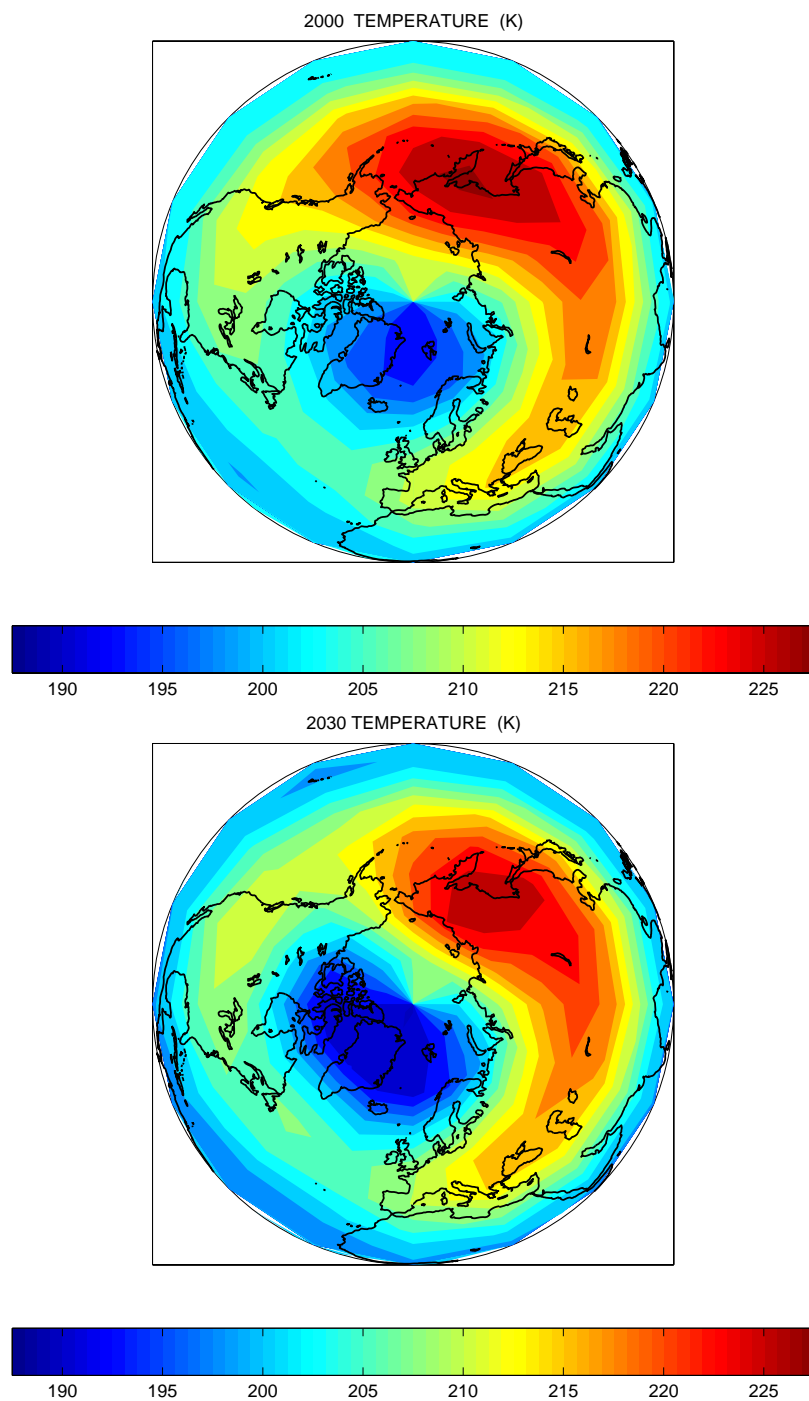


Fig. 11. January averages of the Northern Hemisphere temperature fields (K) at 20 km, for 2000 (top panel, a) and 2030-TC (bottom panel, b).

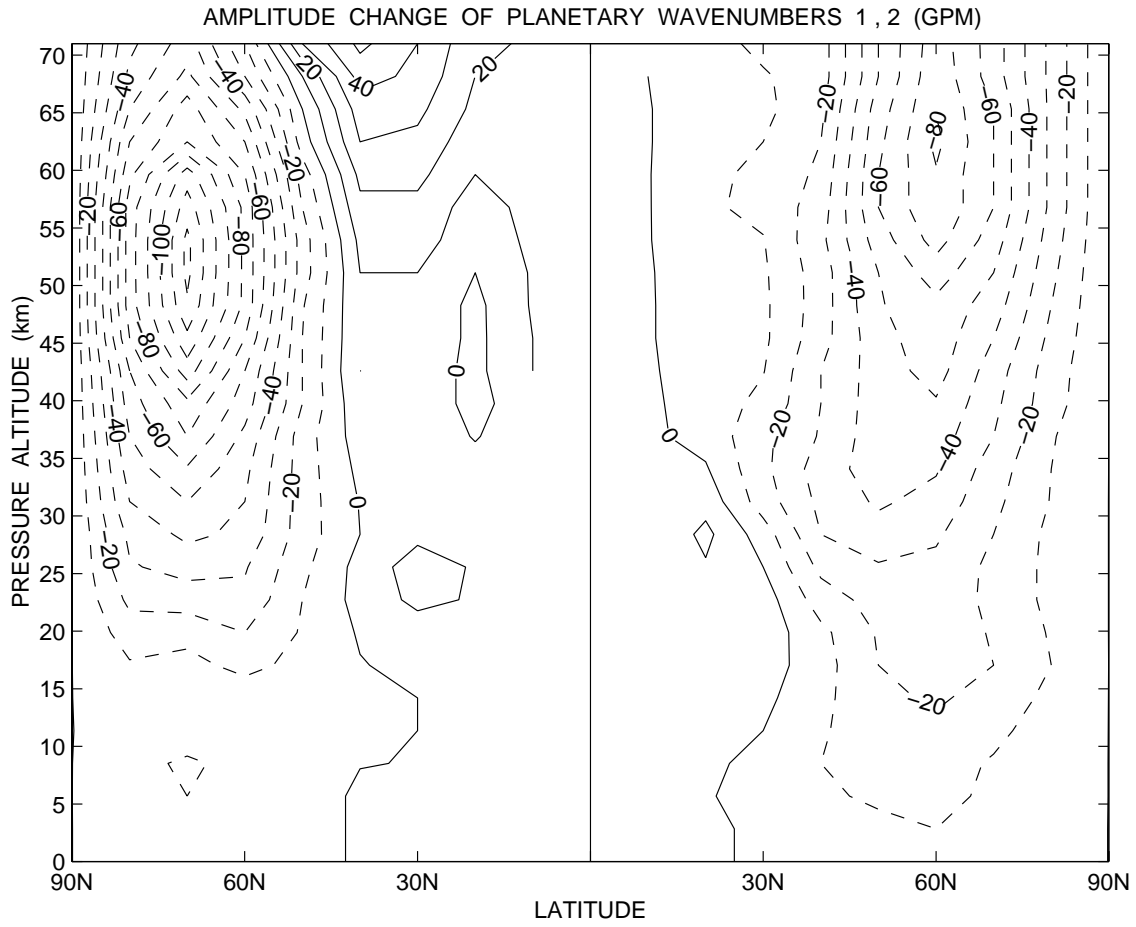


Fig. 12. Calculated Northern Hemisphere anomalies (2030-2000) of the amplitude of geopotential wavenumber 1 (left) and 2 (right) averaged over December, January, and February winter months (gpm). Solid/dashed lines are positive/negative values, respectively. Contour line spacing is 10 gpm.

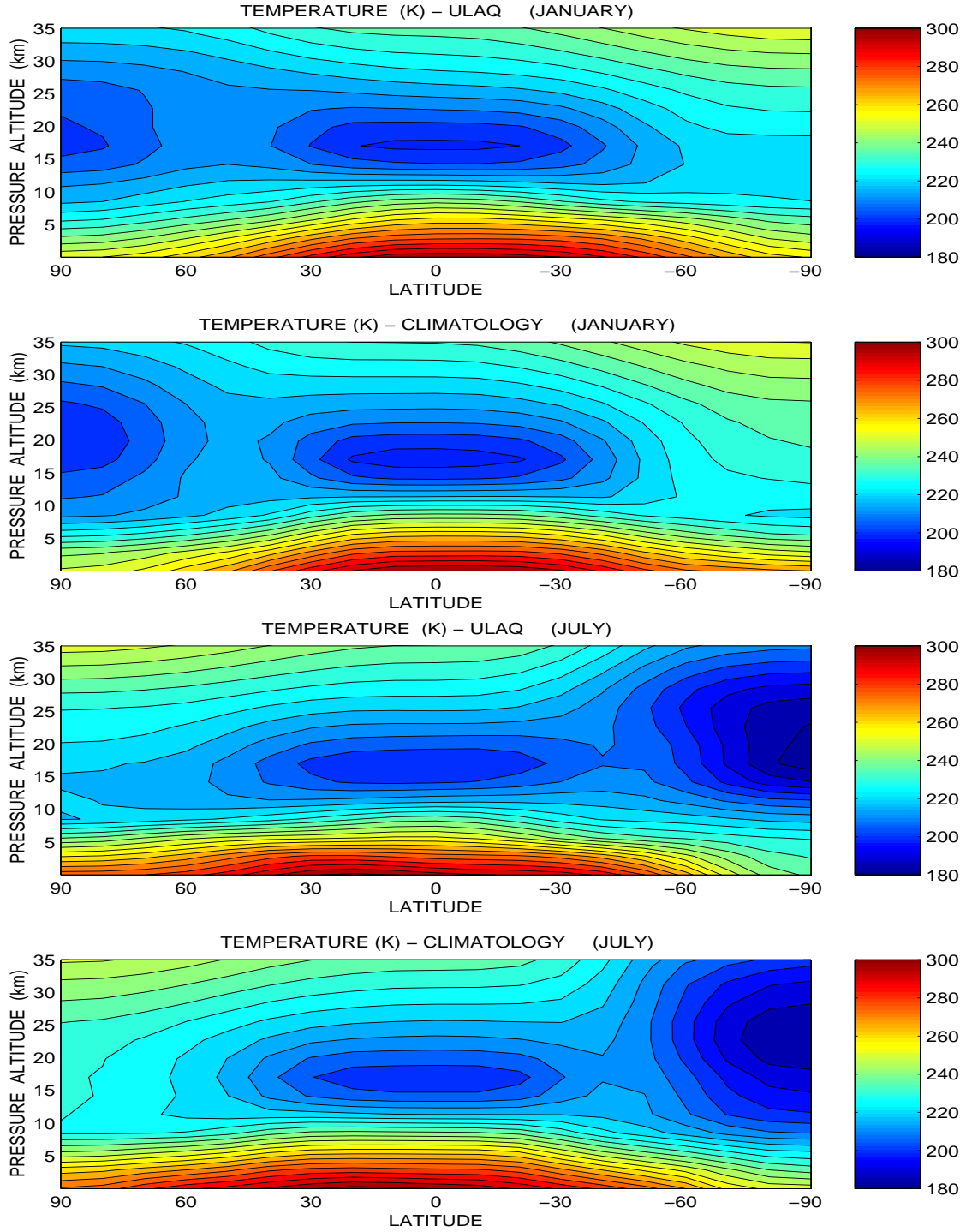


Fig. 13. Monthly and zonally averaged temperatures (K), for January (top panels a, b) and July (bottom panels c, d). Panels (a, c) show the ULAQ-GCM predictions (2000); panels (b, d) show data from the National Meteorological Center (NMC) climatology (1979 to 1995) (update of Randel, 1992). The contour line step is 0.5 K.

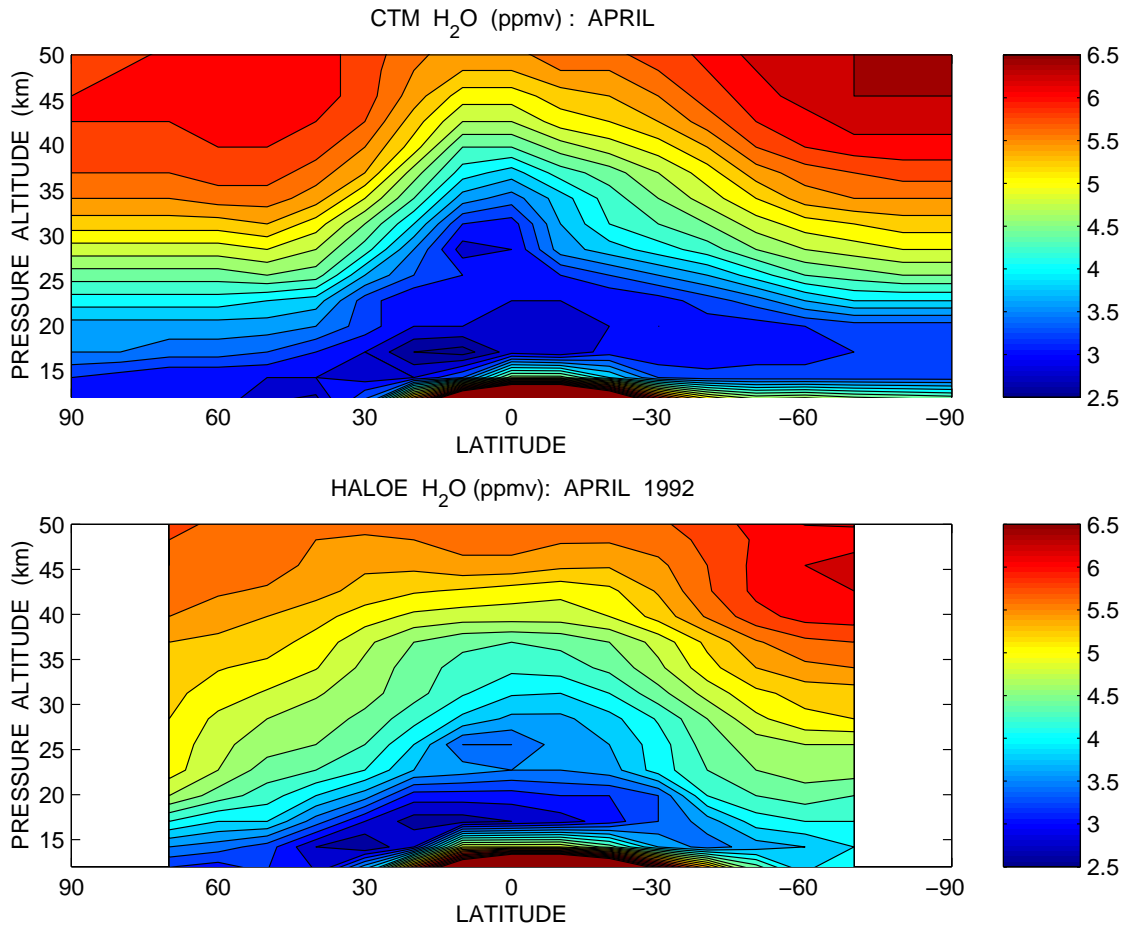


Fig. 14. April 1992 zonal average of H_2O mixing ratios (ppmv). Top panel (a) is for CTM results using a circulation appropriate for 1992 (Pitari, 1993); bottom panel (b) is for HALOE measurements averaged over April 1992 (NASA, 1999). Contour line step is 0.2 ppmv.

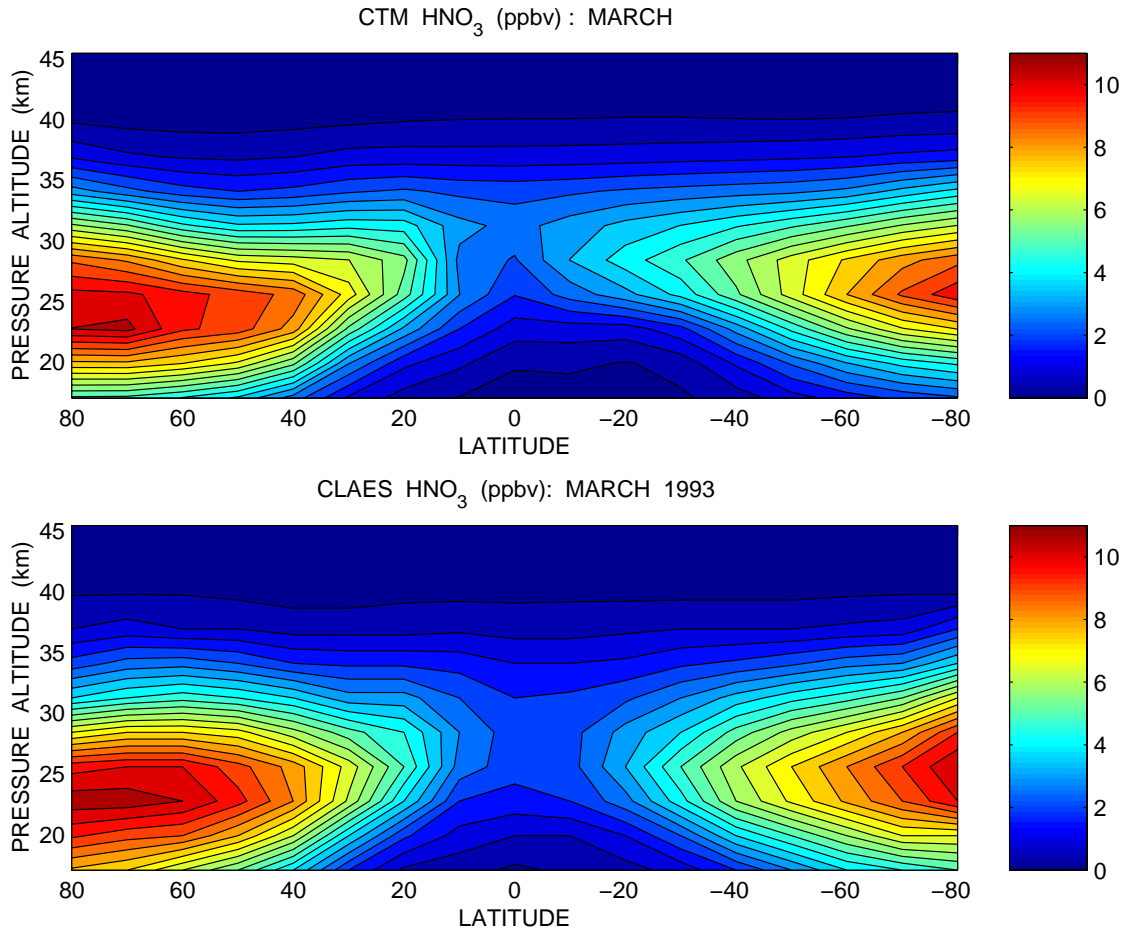


Fig. 15. March 1993 zonal average of HNO_3 mixing ratios (ppbv). Top panel (a) is for CTM results using a circulation appropriate for 1993 (Pitari, 1993); bottom panel (b) is for CLAES measurements averaged over March 1993 (NASA, 1999). Contour line step is 0.5 ppbv.

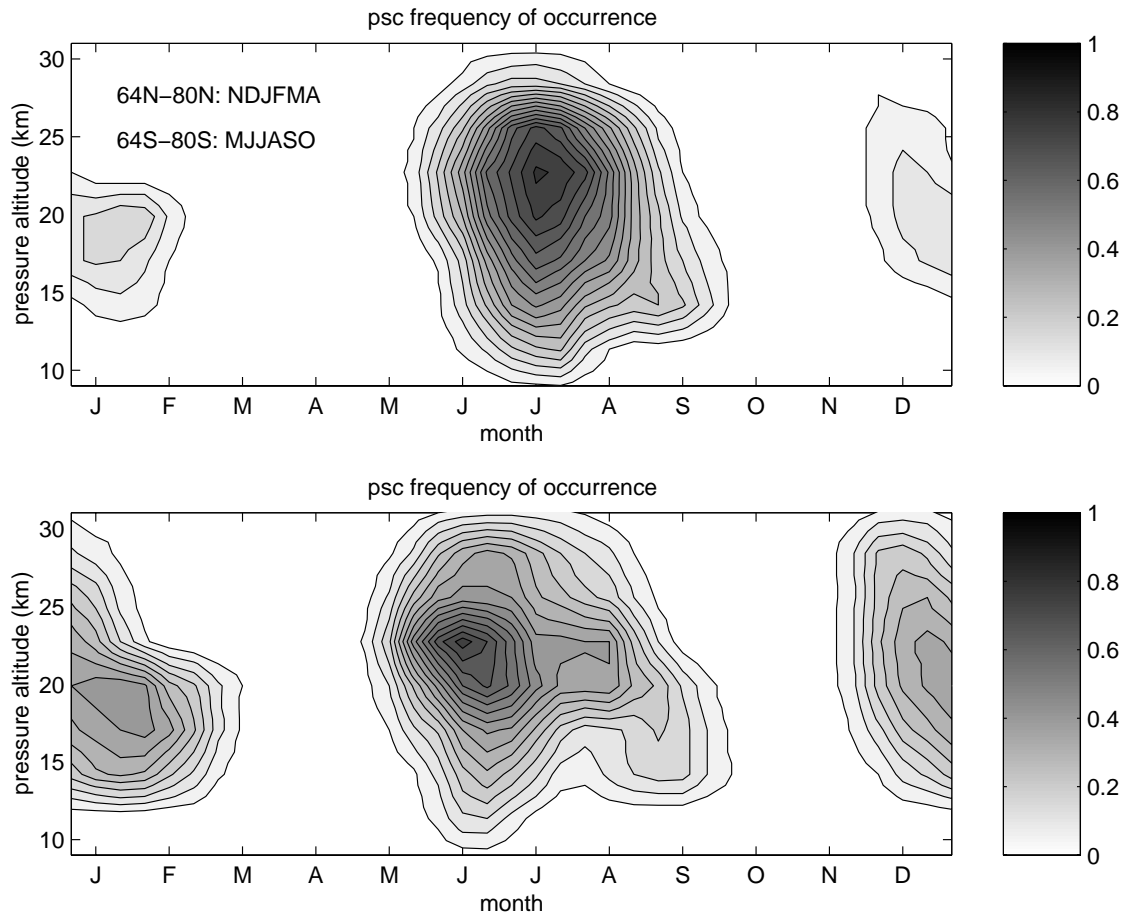


Fig. 16. Time series of calculated PSC frequency of occurrence in Arctic (NDJFMA) and Antarctic regions (MJJASO). Top panel (a) is for 2000, bottom panel (b) for 2030-TC simulation. Values are averaged between 64 and 80 latitude, that is the same band covered by SAM II observations (WMO, 1992). Contour line step is 0.05.

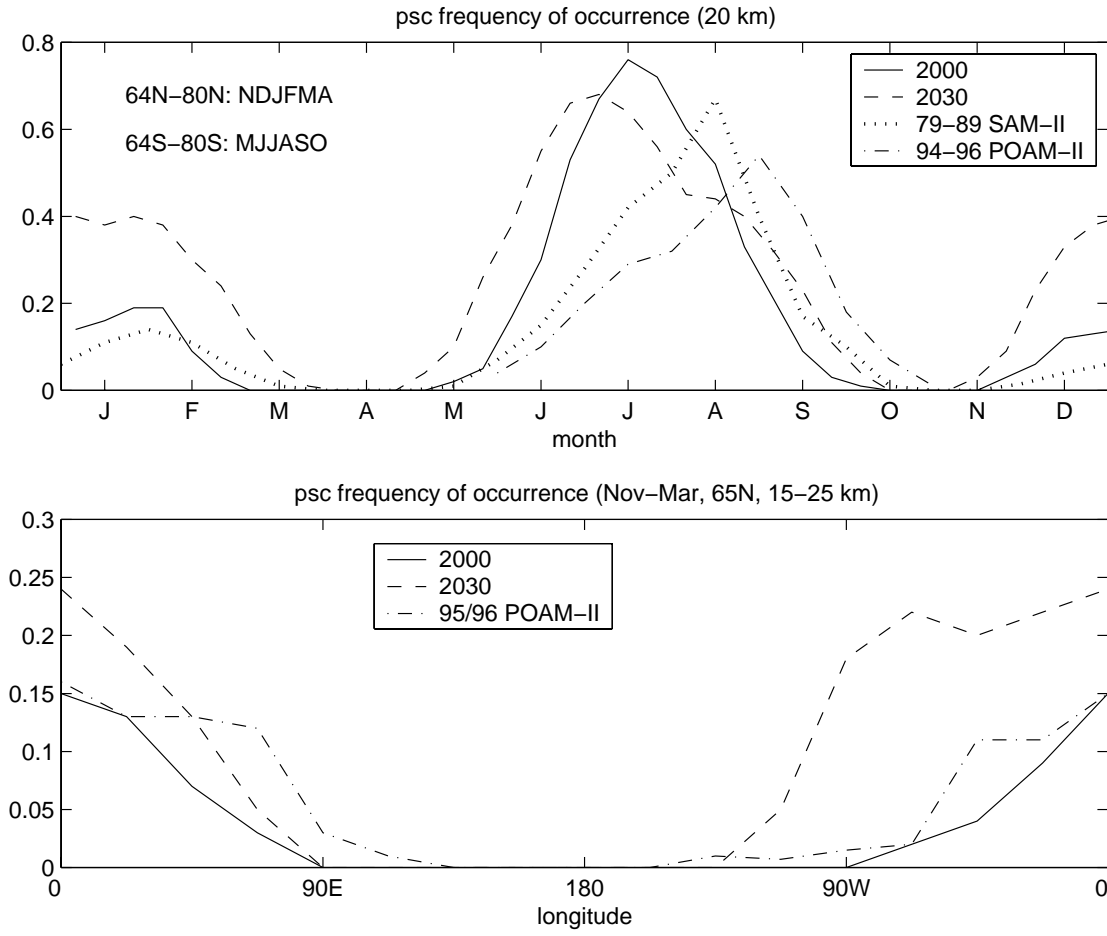


Fig. 17. Top panel (a): time series of PSC frequency of occurrence at 20 km altitude for both Arctic (NDJFMA) and Antarctic regions (MJJASO). Solid line is for present time conditions (2000), dashed line for 2030-TC simulation, dotted line for 1979-89 SAM-II observations (WMO, 1992), dash-dotted line for POAM-II observations (WMO, 1999). Bottom panel (b): NDJFM averaged PSC frequency at 65N latitude in the 15-25 km altitude layer, as a function of longitude. Solid and dashed lines are for 2000 and 2030-TC simulations, respectively, dash-dotted line for POAM-II observations (<http://opt.nrl.navy.mil/POAM/>; Fromm et al., 1999).

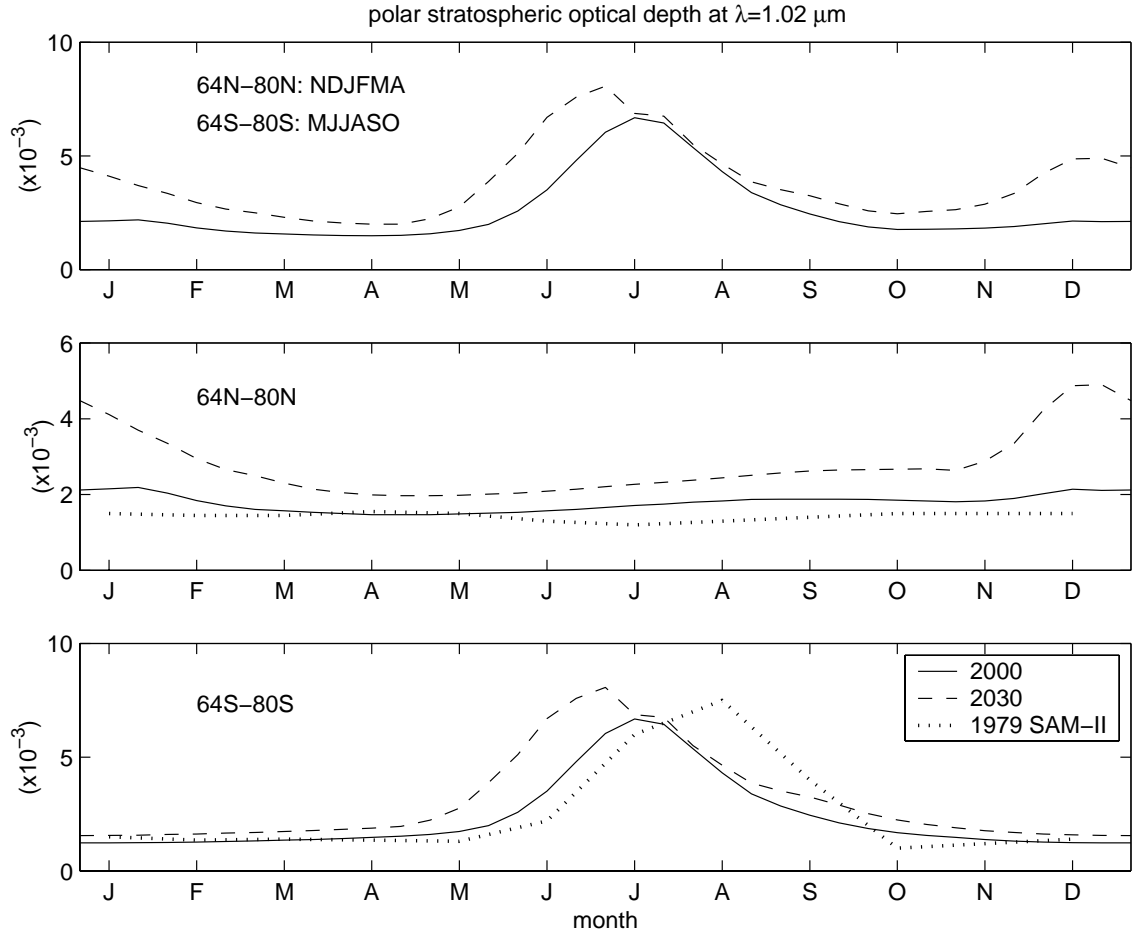


Fig. 18. Time series of $1.02 \mu\text{m}$ polar stratospheric optical depth in the 64-80 latitude band and calculated from 2 km above the tropopause. Top panel (a) is for both Arctic (NDJFMA) and Antarctic regions (MJJASO), center panel (b) is for the Arctic, bottom panel (c) for the Antarctic region. Solid lines are for present time conditions (2000), dashed lines for 2030-TC simulation, dotted lines for 1979 SAM-II observations (McCormick and Wang, 1987).

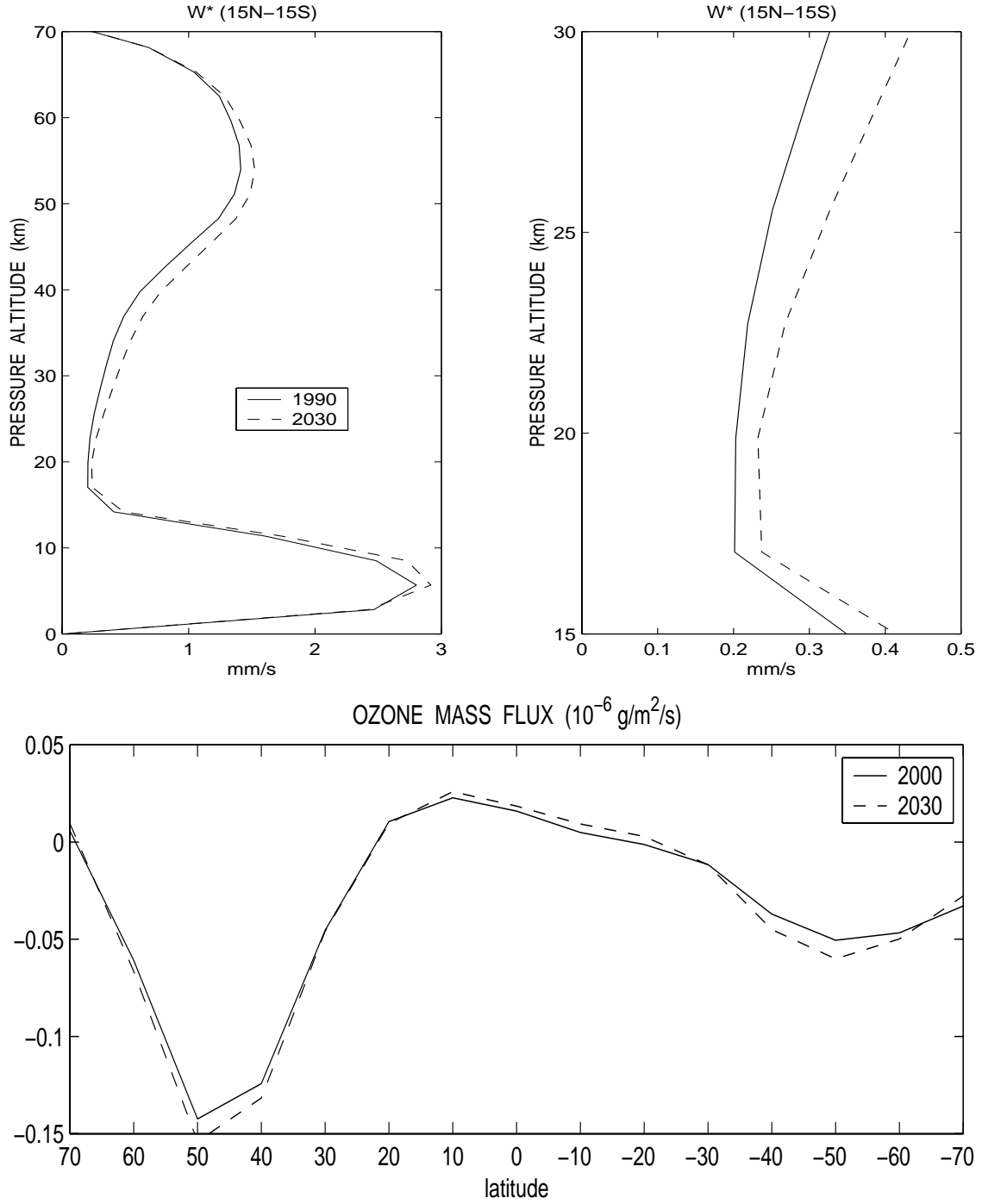


Fig. 19. Mean annual residual vertical velocity (\bar{w}^*) averaged between 15N and 15S (top left panel, a). Solid line is for 2000, dashed line for 2030 (experiment 'TC'). Units are mm/s. Top right panel (b) is an inset of (a) in the lower stratosphere (15-30 km altitude). Bottom panel (c) shows the calculated vertical ozone mass fluxes at 100 hPa for 2000 and 2030-TC (solid and dashed lines, respectively) keeping the ozone field fixed to year 2000 conditions. Units are $10^{-6} \text{ g m}^{-2} \text{ s}^{-1}$.

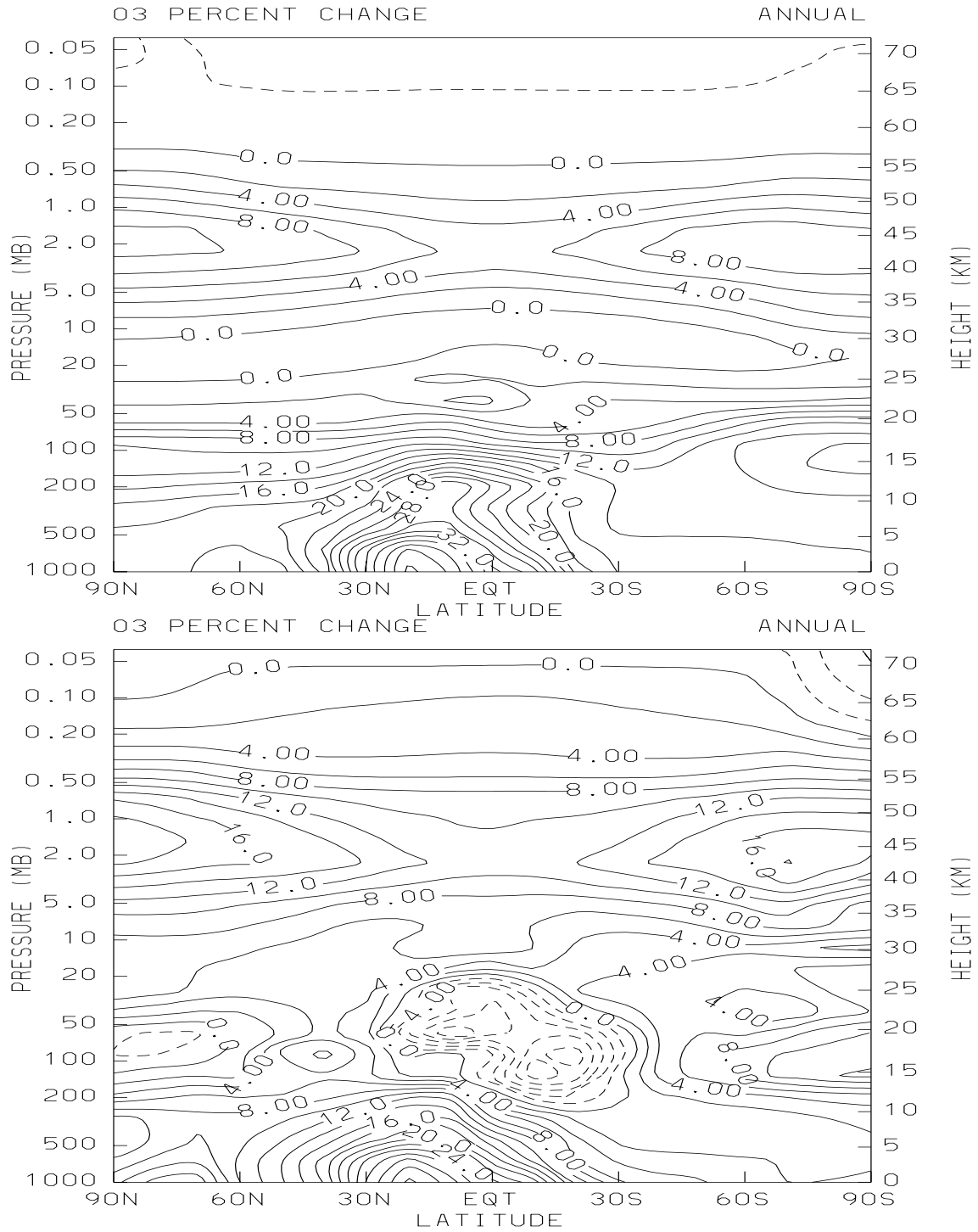


Fig. 20. Calculated zonally and annually averaged ozone profile change for year 2030 with respect to 2000: top panel (a) is for experiment 'CH' (i.e. updated chemistry, fixed SO_2 surface fluxes, fixed climate); bottom panel (b) is for experiment 'TC' (i.e. updated chemistry, SO_2 fluxes and climate). Contour line spacing is 2%.

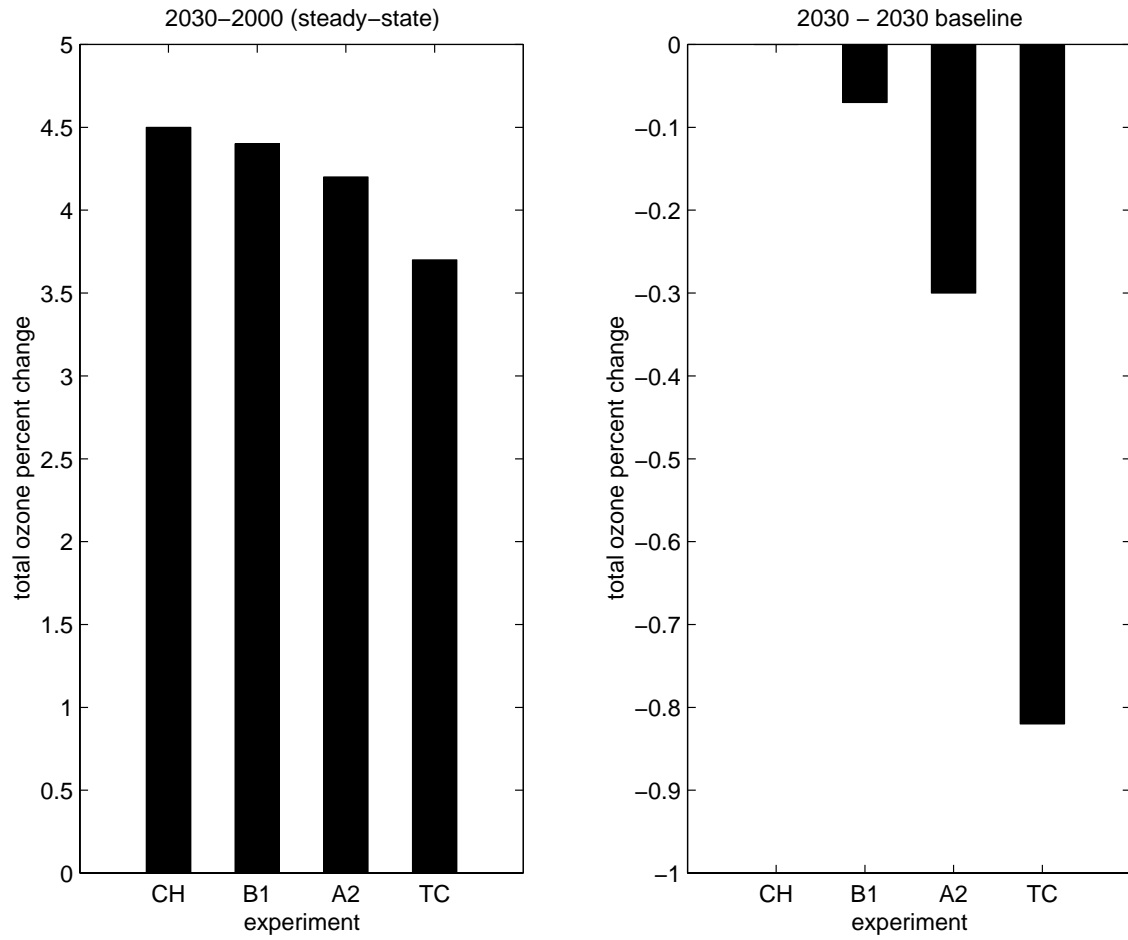


Fig. 21. Calculated steady-state total ozone column percent changes (90S-90N global annual mean) in the different future scenarios for 2030-2000 (left panel, a) and for 2030 with respect to ‘CH’ case (i.e. chemistry update alone) (right panel, b). See Table 1 for a description of the numerical experiments.